Effects of Ligand Substituents in a Family of Fe(II) Spin Crossover Complexes

Ahmed Ahmed

Submitted in accordance with the requirements for the degree of Master of Science by Research

The University of Leeds

School of Chemistry

September 2018

Acknowledgements

I would like to thank Professor Malcolm Halcrow for the opportunity to work within the group, his experience and knowledge has been of great help to me throughout the project.

I would like to thank members of the technical staff for their assistance and training. I would like to thank Mr. Simon Barrett and Dr. Mark Howard for carrying out variable temperature NMR experiments, Dr. Chris Pask for X-ray diffractometer training and assistance and Dr. Raf Kulmaczewski for carrying out SQUID magnetometry measurements.

I would like to express my gratitude to the members of the Halcrow, McGowan and Hardie groups for both their camaraderie and chemical wisdom. A special thank you to Izar Capel for his regular bets that motivated me and Sam Greatorex for his understanding of the Irish craic. I would also like to thank Raf and Jonny Fowler for our regular football talks.

I special thank you to my friends and family who shown me love and support over the past year.

Abstract

Seven different 2,6-di(1*H*-pyrazol-1-yl)pyridine ligands were synthesized from 4-cyano-2,6-dichloropyridine and 4-methyl-2,6-dichloropyridine and complexed with Fe(II) salts. The spin state of the subsequent materials has been investigated in both the solution and solid state. 4-Halopyrazolyl Fe(II) bpp complexes show anomalous behavior in solution where their spin state appears intermediate between that of high spin and low spin, this has been attributed to decomposition of their complexes in solution. In the solid state the $[Fe(bpp)_2][X]_2$ salts have shown the ability to undergo thermal spin crossover. Salts that pack in a specific motif known as a terpyridine embrace undergo spin crossover with hysteresis with remarkable consistency whilst those that do not remain low spin .

Contents

Chapter one: Introduction

Chapter Two: Results and Discussion

List of Abbreviations

Δ_{oct}	Ligand Field Strength
Π	Electron Pairing Energy
HS	High Spin
LS	Low Spin
SCO	Spin Crossover
LIESST	Light Induced Excited Spin State Trapping
$T_{1/2}$	Spin Crossover Midpoint
Bpp	2,6-di(1*H*-pyrazol-1-yl)pyridine
UV	Ultra Violet
Me	Methyl
Mes	Mesityl
δ	Chemical shift in parts per million
NMR	Nuclear Magnetic Resonance
SQUID	Superconducting Quantum Interference Device
hfac	hexafluoroacetylacetonato

List of Figures

List of Schemes and Tables

Ligands

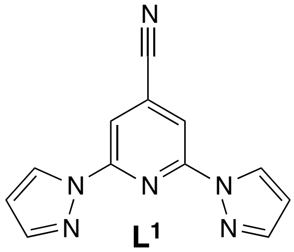

L^{1}

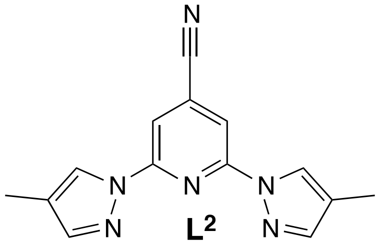

L^{2}

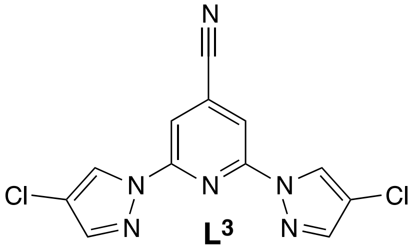

L^{3}

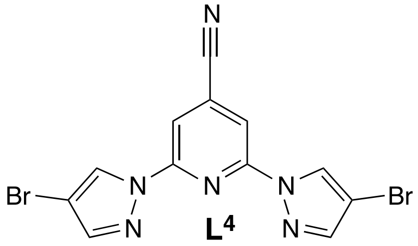

L^{4}

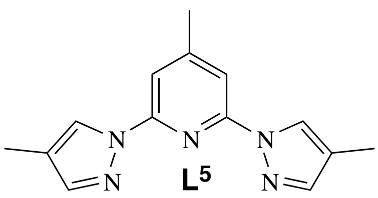

L^{5}

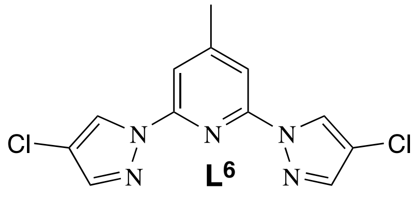

L^{6}

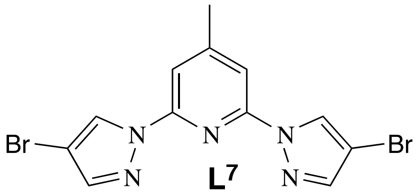

L^{7}

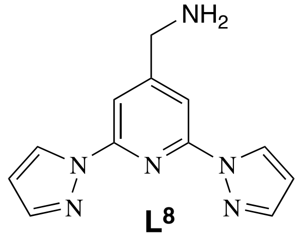

L^{8}

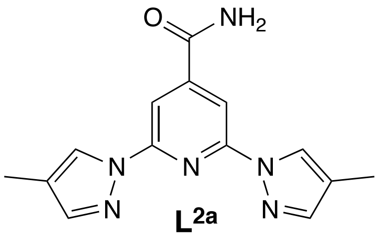

L^{2a}

List of Complex Salts

[Fe(**L**^{1})$_2$][X]$_2$	X=BF_4^- (**1a**) X= ClO_4^- (**1b**) X= OTf^- (**1c**)	[Fe(**L**^{5})$_2$][X]	X= BF_4^- (**5a**) X= ClO_4^- (**5b**) X= OTf^- (**5c**)
[Fe(**L**^{2})$_2$][BF_4]$_2$	**2**	[Fe(**L**^{6})$_2$][BF_4]$_2$	**6**
[Fe(**L**^{3})$_2$][BF_4]$_2$	**3**	[Fe(**L**^{7})$_2$][BF_4]$_2$	**7**
[Fe(**L**^{4})$_2$][BF_4]$_2$	**4**	[Fe(**L**^{8})$_2$][ClO_4]$_2$	**8**

Chapter One: Introduction

1.1 Crystal Field Theory

Crystal field theory describes bonding in transition metal complexes through the electrostatic repulsion of metal d-orbitals and a static electric field produce by ligand non-bonding electrons. The theory was developed by Bethe and Van Vleck in 1932.[1] The five metal d-orbitals are degenerate in a free ion and increase in energy when place in a spherical electric field. The two most common geometries observed are octahedral and tetrahedral. In an octahedral electric field, the d orbitals experience different magnitudes of electrostatic repulsion for the ligand donor orbitals, resulting in the breaking of the degeneracy.

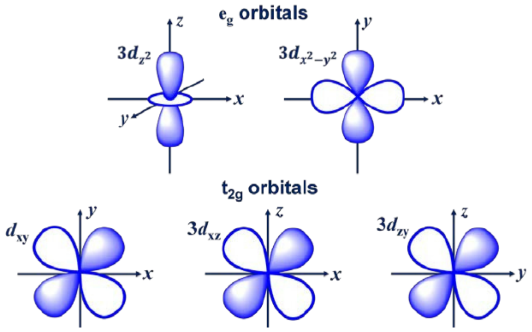

Figure 1 3d-orbitals

The ligand donor orbitals approach from the six corners of the octahedron. The d_{z^2} and $d_{x^2-y^2}$ orbital lie on the axes of ligand approach while the d_{xz}, d_{yz} and d_{xy} orbitals lie in between the axes and thus feel less electrostatic repulsion (figure 1). This leads to the formation of two distinct groups of energy levels, the doubly degenerate e_g and the triply degenerate t_{2g} in an octahedral crystal field. The difference in energy between the t_{2g} and e_g is known as the crystal field splitting energy (Δ_{oct}). The magnitude of Δ_{oct} is affected by many factors including the nature and oxidation state of the metal ion and the nature of the donors. Ligands that produce a large Δ_{oct} are known as strong field ligands, while those that produce a small Δ_{oct} are known as weak field ligands. An empirically derived series can be obtained for a given metal in which donors are arranged by the magnitude of Δ_{oct}, this is known as the spectrochemical series.[2,3]

$$I^- < Br^- < Cl^- < OH^- < RCO_2^- < F^- < H_2O < NCS^- < NH_3 < en < phen < CN^- < CO$$

In a tetrahedral crystal field the d_{xz}, d_{yz} and d_{xy} orbitals lie closest to the approaching ligands and thus experience greater electronic repulsion than the d_{z^2} and $d_{x^2-y^2}$ orbitals. Thus in a tetrahedral crystal field the t_2 energy level is higher in energy than the e_g. CFT can account for properties such as colour but does not sufficiently describe the bonding in transition metal complexes.

1.2 Ligand Field Theory

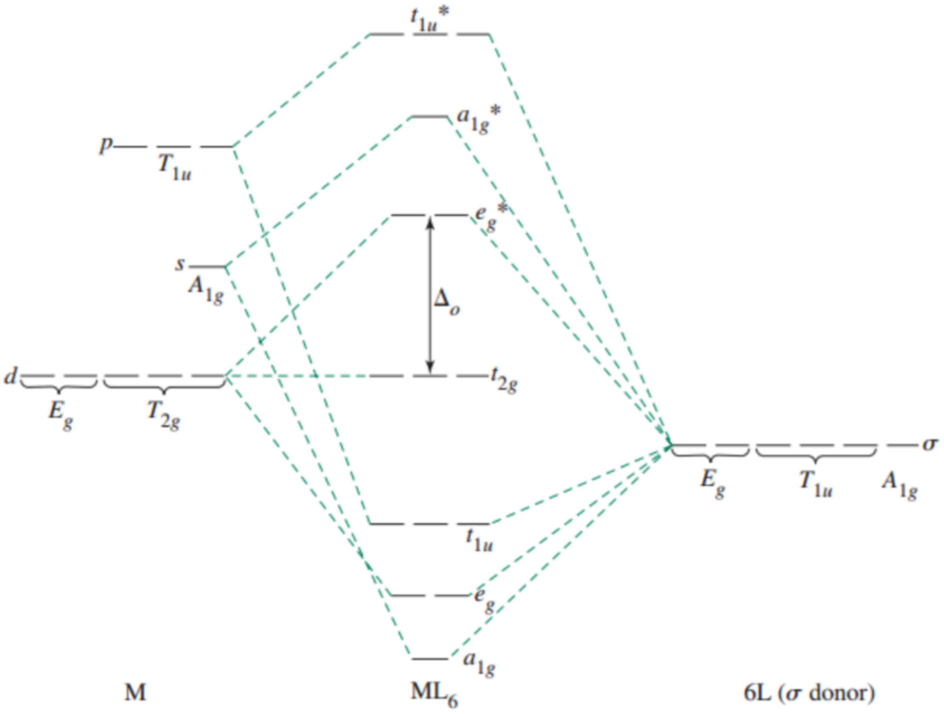

Figure 2 Molecular orbital diagram for octahedral complexes

Ligand field theory (LFT) describes the bonding in transition metal complexes through the use of molecular orbital theory and is thus a more accurate model. LFT factors in the symmetry and energy of both ligand and metal orbitals. This approach allows for the forming of both bonding and anti-bonding metal complex orbitals derived from the metal and ligand orbitals. The d_{xz}, d_{yz} and d_{xy} orbitals form the triply degenerate t_{2g} set from π- type interactions with the ligand orbitals,[4] while the $d_{x^2-y^2}$ and d_{z^2} orbitals form the doubly degenerate e_g^* molecular orbitals from σ-type overlap with ligand orbitals (figure 2). As the e_g^* set are anti-bonding orbitals population of these orbitals with electrons destabilizes the complex and results in larger M-L bond lengths. Interactions between ligand π orbitals and the metal orbitals make the greatest contribution to Δ_{oct}. π Donor ligands with filled π orbitals will interact weakly with the metal t_{2g} orbitals resulting in a small Δ_{oct}. π Acceptor ligands with low lying empty π^* orbitals at a similar energy level have a large overlap with the t_{2g} set leading to a large Δ_{oct}.

1.3 Spin States and Spin Crossover

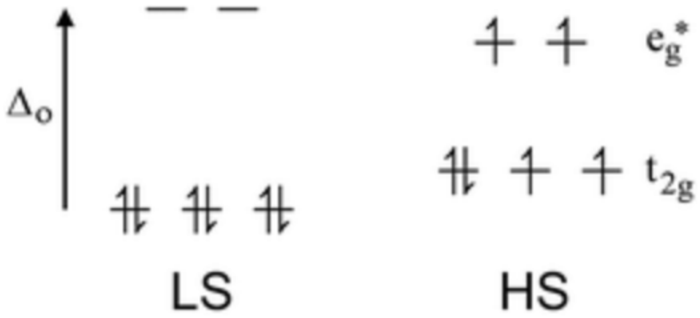

Figure 3 High spin and low spin electronic configurations for d^6 ions

In octahedral d^4-d^7 ions the t_{2g} and e_g^* energy levels can be populated in two different ways depending on the magnitudes of Δ_{oct} and the electron pairing energy (Π) (figure 3). When Δ_{oct} is lower than Π electrons will occupy the e_g^* orbitals before doubly populating the t_{2g} resulting in an ion with the maximum number of unpaired electrons called the high spin (HS) state. Conversely when Δ_{oct} is much greater than Π then electrons will pair in the t_{2g} set before populating the e_g^* set resulting in the minimum number of unpaired electrons, called the low spin (LS) state. If the difference in energy between Δ_{oct} and Π is sufficiently small then external stimuli may cause a reversible transition from HS to LS or vice versa. This phenomenon is known as spin crossover (SCO). SCO may be caused by heat, pressure, a magnetic field or irradiation of light with appropriate wavelength.[5,6,7] SCO was first observed in 1931 by Cambi and Szego in a family of tris-dithiocarbamate Fe(III) complexes.[8] SCO has many effects associated with it such as changes to molecular bond length, colour, electrical resistivity and magnetic susceptibility.[9] Thus there are many ways to study SCO with magnetic measurements and X-ray diffraction being the most common.

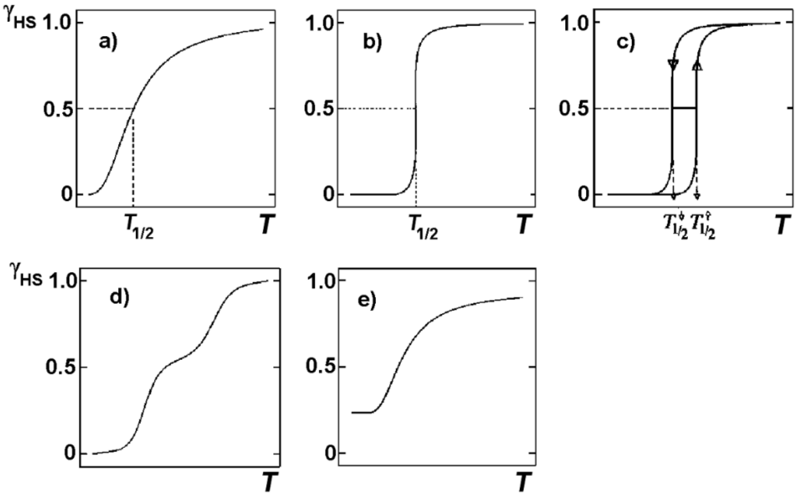

Figure 4 Types of SCO, plot of high spin fraction γ_{HS} vs Temperature T: a) gradual b) abrupt c) with hysteresis d) two-step e) incomplete

There are five different types of SCO, differing in their cooperativity (the ability of one center undergoing SCO to communicate this to another (figure 4)).[10] When cooperativity is low gradual SCO is observed with the metal centers undergoing SCO over a broad temperature range. When cooperativity is higher abrupt transitions may be observed with all centres undergoing SCO in a small temperature range usually under 10 K.[11] SCO with hysteresis occurs when cooperativity is highest. Hysteresis is when changes in a physical property lag behind the changes in the effect causing it. For example, thermal hysteresis occurs when the temperature of transition on heating is different to the temperature of transition on cooling. Thus a magnetic bistability exists within the hysteresis loop temperature range where both the HS and LS state can exist simultaneously. This bistability can have a memory effect and thus has potential to be used in data storage.[12] One possible explanation for hysteresis is if there is a structural phase change in the lattice associated with the transition,[13] another is mechanical interactions occurring from intermolecular π-π stacking.[14] Two-step SCO is quite rare, but can occur in dinuclear complexes where SCO in one metal center makes SCO in the other less favorable and thus occur at a different temperature. Incomplete transitions occur when SCO at some metal centres prevent SCO from occurring in other metal centres. An important parameter for studying SCO is $T_{1/2}$ or the temperature of transition, this is the temperature where the populations of both HS and LS state are equal.

1.4 Thermodynamics of SCO

The thermodynamics of SCO are described by the Gibbs Free energy equation with the ground state having the lowest Gibbs free energy.[15] The HS state will have higher entropy due to having a higher spin degeneracy and larger vibrational entropy contribution, thus the HS state dominates at higher temperatures.[16] The LS state will have a larger enthalpy due to having fewer populated antibonding orbitals and will thus be favoured at lower temperatures. The two states for a single molecule can be modelled using two potential energy wells with the Fe(II) LS state having a $^1A_{1g}$ term and the HS state having a $^5T_{2g}$ term (figure 5).[13] The x-axis is a measure of Fe-L bond distance with the HS state being the ground state at longer bond distances. The two potential energy wells describe the vibrational energy levels of the LS and HS states. As the internuclear distance increases a system crossing occurs and the HS state then becomes the ground state. Thus for thermal SCO the higher LS vibrational energy levels are populated as the sample is heated, eventually the point is reached where transition to the HS zero point energy is more favorable. The difference between the two states zero point energy is denoted ΔE_{HL} and described by the equation $\Delta E_{HL} = K_bT$ where K_b is the Boltzmann constant and T is the temperature in Kelvin. Thus in dilute systems such as solutions or materials doped with non-SCO ions the spin states will be observed in the Boltzmann distribution.[17]

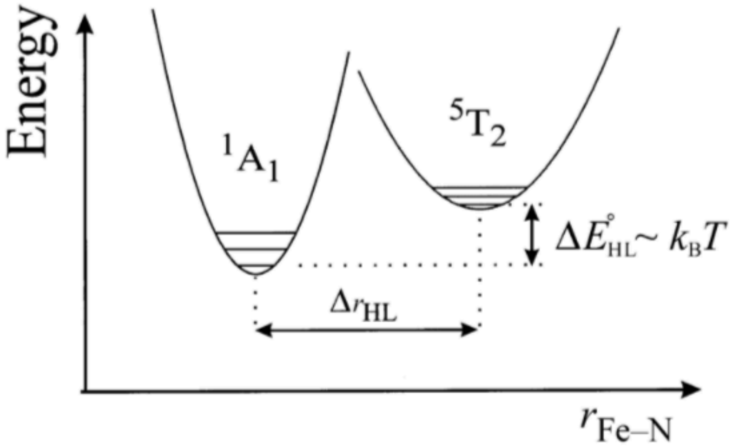

Figure 5 Potential energy wells for Fe(II) LS $^1A_1$ and HS $^5T_2$ states where r is the Fe-N bond length

From figure 5 it follows that some materials can be kinetically trapped in the HS state if there isn't sufficient energy to undergo intersystem crossing to the LS state. This is the basis of the LIESST (light induced excited spin state trapping) phenomenon. LIESST is observed when a complex is irradiated with light of appropriate wavelength to induce SCO, the sample is kept at a very low temperature preventing it from undergoing SCO and thus the metastable HS state is trapped.[13,18] The sample is then slowly heated and eventually relaxes to the thermodynamically stable LS state. If the sample is not warmed the only available pathway for relaxation is quantum tunneling which can be very slow due to the difference in atomic coordinates for the HS and LS states.[19]

1.5 SCO in Fe(II)

SCO is most widely reported in Fe(II) systems with the first examples being Fe(II)-bis(1,10-phenanthroline) di-cyanate complexes reported in 1967 by Konig and Madeja.[20] SCO in Fe(II) involves a transition from the diamagnetic LS state with S=0 to the paramagnetic HS state with S=2. The change from the LS state with a magnetic susceptibility (χT) of 0 cm^3 mol^{-1} K to the HS state with a χT of approximately 3.5 cm^3 mol^{-1} K is easily detectable by magnetometry. Typically an N_6 donor set is used to promote SCO in Fe(II) complexes. There are large changes in M-L bond lengths associated with SCO with LS Fe-N bond lengths typically between 1.8- 2.1 Å, with HS Fe-N bond lengths typically between 2.1- 2.4 Å. It is worth noting that the HS state is Jahn-Teller active which may lead to angular distortions of the coordination geometry.[21] These changes are detectable by X-ray crystallography, IR and Raman spectroscopy.[22] The large changes in M-L bond lengths can have pronounced effects on the ligand structure such as causing conformational changes which then propagate throughout the lattice. This is a large factor in why most cooperative transitions are seen in Fe(II) systems.[23] These changes can affect the shape of the molecule as well, with HS complexes having a wider range of geometries and greater distortions from ideal octahedral geometry.[24] For planar meridional tridentate ligands such as 1-bpp (2,6-bispyrazoylpyridine) the dihedral angle θ between the two ligand planes can be used to quantify the distortions from 90° (figure 6).[24] Typically in the LS state θ tends to be close to 90° with HS values deviating greatly. The angular Jahn-Teller distortion parameter ϕ which is a measure of the trans $N_{pyridyl}$ – Fe- $N_{pyridyl}$ bond angle and is usually 180 ° in LS complexes with smaller values for HS complexes.

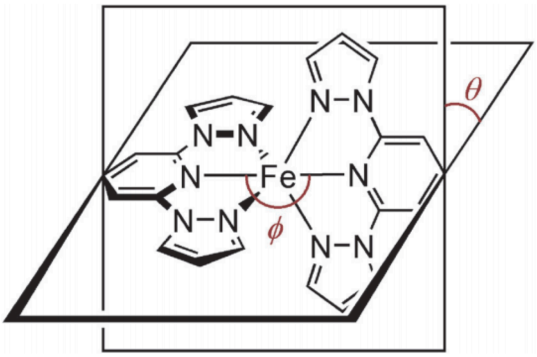

Figure 6 Octahedral distortion parameters θ and ϕ for $[Fe(bpp)_2]^{2+}$

When there are large differences between the HS and LS states geometries complexes can remain HS at temperatures studied as the rigid lattice will not allow for the large structural changes require to undergo SCO.[25] A similar effect can be seen when bulky ligand substituents or twisted ligand conformations are present sterically trapping the complex in HS state.[26] Currently the most cooperative materials reported are mononuclear molecular compounds.[27] However many SCO Fe(II) 1 and 2-dimensional coordination polymers have also been reported.[28,29] An $[Fe(Htrz)_3](ClO_4)_2$ polymer where (Htrz =1,2,4- 1H-triazole) (figure 7) has been shown to undergo thermal SCO with a 40 K wide hysteresis loop centred around 296 K when a drop of water is added. This large cooperativity arises from both the covalent bridging of Fe(II) ions by the triazole ligands, and hydrogen bonds in the lattice.[30]

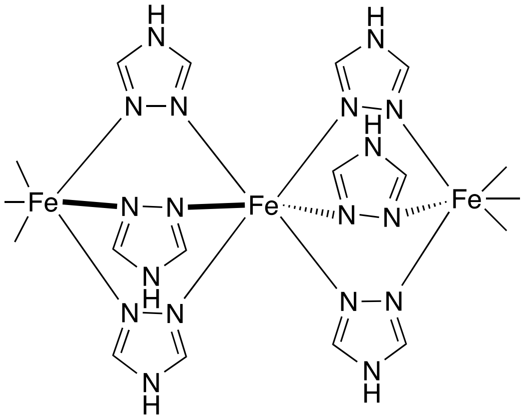

Figure 7 Structure of $[Fe(Htrz)_3](ClO_4)_2$ polymer repeating unit

Polymorphism is also observed for some SCO materials whereby the material can exist in two or more crystalline forms.[31] Different polymorphs will have different molecular arrangements or conformations and thus differ in their cooperativity, some materials may have both SCO active and inactive polymorphs.[32] Thus control of the crystallization process is a vital area of ongoing research.[33] Lattice defects also greatly affect the material, usually decreasing the cooperativity and leading to gradual transitions and smaller hysteresis loops.[34] Powder X-ray diffraction is a powerful tool in this regard as it can be used to determine the presence of polymorphs or solvates in the absence of single crystal diffraction data.[35]

1.6 SCO in Solution

SCO in solution is more representative of the individual molecule's behaviour than solid state SCO, due to the absence of lattice effects, making it a good tool for studying ligand substituent effects on spin states. In solution the populations of both the HS and LS states will be determined by the Boltzmann distribution explaining why transitions observed are typically gradual.[13] However there are various other effects that must be taken into account such as choice of solvent, anion loss or exchange, additives, isomerizations and ligand displacements.[36,37,38] Weakly interacting solvents such as acetone and nitromethane are ideal as they will not greatly affect the spin state while strongly interacting solvents such as water will stabilise the LS state and shift the value of $T_{1/2}$ to a higher temperature if they don't hydrolyse the complex.[39] This indicates that hydrogen bonding between solvents and ligand moieties can greatly affect the spin state. Ligand dissociation has been shown to allow for SCO with an example being $[Fe(BPMEN)(CH_3CN)_2][ClO_4]_2$ (BPMEN= *N*^{1},*N*^{2}-bis(pyridin-2-ylmethyl)ethane-1,2-diamine) where the equilibrium of HS-LS states is dependent on the loss or gain of coordinated acetonitrile.[40] Complexes in solution are more flexible than the solid state and so can adopt a broader range of geometries. Thus some complexes undergo SCO in solution but not in the solid state.[41] In the absence of sterically demanding ligands SCO in solution is almost purely influenced by Δ_{oct}, with solvent effects also present this makes solution studies ideal for the study of ligand electronic properties.[42]

^{1}H-NMR spectroscopy is the most common method of studying SCO materials in solution, providing both structural and magnetic insights into the nature of species in solution. Signals for protons near a paramagnetic ion such as HS Fe(II) tend to have chemical shifts in the region between 0-100 ppm. The signals are also broadened due to coupling between the paramagnetic ions unpaired electron magnetic moments and that of the ^{1}H nuclei. The relaxation rate of protons coupled to the unpaired electrons is much faster than for J-coupling, so a broadened peak is observed.[43] Variable temperature ^{1}H-NMR can then be used to measure the paramagnetism of a species in solution, which is known as Evan's method.[44] This is carried out by dissolving the sample to be measured with a reference molecule such as tetramethylsilane (TMS) in the solvent of choice. A special insert tube containing only the reference molecule and solvent is also inserted within the NMR tube. The VT experiment is then carried out with the change in shift of the reference proportional to the population of the HS state. The $\chi_M T$ value can be obtained from the diamagnetic shifts of the solvent molecules interacting with the paramagnetic species as the diamagnetic susceptibility of the solvent is negligible.[45] Of greater importance is correcting for the density changes of the solvent with temperature.[46] Limitations of the technique arise from sample solubility and the temperature range over which the solvent remains liquid. Thermodynamic parameters such as the entropy and enthalpy of transition may also be obtained.[47] UV-Vis spectroscopy is another method for studying SCO in solution with the Fe(II) HS state having much lower absorbance than the LS state due to having a lower number of spin allowed transitions.

1.7 SCO Complexes of Bis-pyrazolylpyridine

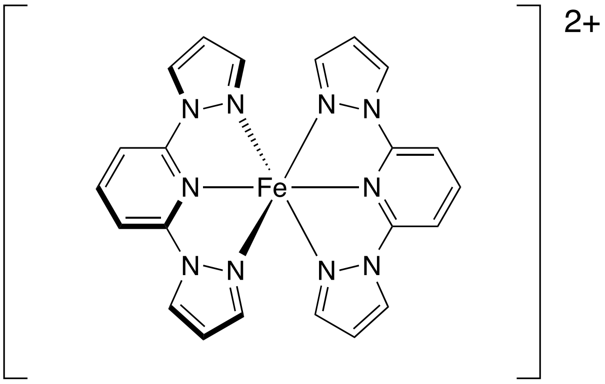

Figure 8 [Fe(bpp)$_2$]$^{2+}$ parent complex

Fe(II) complexes of bpp have been studied extensively, bpp is a tridentate planar ligand with 2 equivalents of bpp per Fe(II) centre generating an N_6 donor set (figure 8). The two ligand arms are at an approximately 90° angle from each other with the complex cation having an idealized D_{2d} symmetry, however there can be large deviations from this angle especially in the HS state.[21] Bpp ligands are easily functionalized by using the desired pyridine and pyrazoles precursors.[48] The pyrazolyl donors are weaker σ donors than the pyridyl donors.[49] Many Fe(II) complexes of bpp ligands have been shown to undergo SCO. The planar heterocyclic rings for bpp ligands allow for π-π stacking, increasing the interactions by extending the aromatic rings can lead to increased cooperativity and hysteretic transitions.[50] Ligand substituent on both the pyridine and pyrazolyl rings have been shown to exert strong effects on both the solid and solution phase SCO behavior.[51] In the solid state SCO behavior has also been shown to be greatly affected by the choice of counterion used and the presence of solvent molecules in the lattice.[52,53] Salts of $[Fe(bpp^{Me, H})_2 [X^-]_2$ where (X= BF^-, ClO_4^-, PF_6^-, $CF_3SO_3^-$) have been studied where the tetrafluoroborate and perchlorate salts are isostructural and undergo SCO with hysteresis, whilst the hexafluorophosphate and triflate salts are high spin and low spin respectively. The salts which undergo SCO pack in a terpyridine embrace that is common for 1-bpp complexes which undergo hysteretic transitions.[54] This motif involves offset face-to-face and edge-to-face interactions between the outer pyridyl or pyrazolyl rings (figure 9). The result is the formation of two dimensional layers of complex ions with the ligand arms offset and high cooperativity throughout the material.[55]

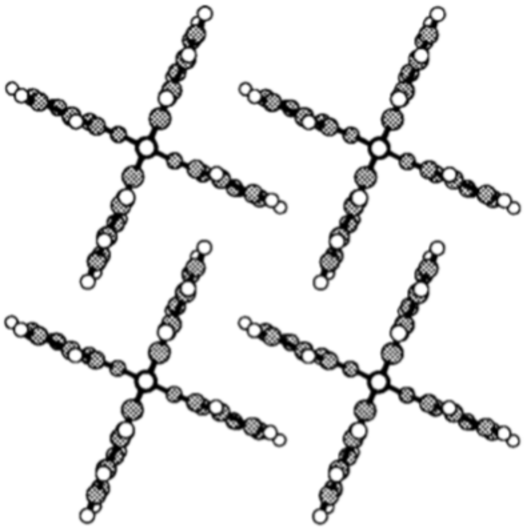

Figure 9 Schematic of terpyridine embrace of $[Co(terpy)_2]^{2+}$ cations

The tetrafluoroborate salt of the parent complex $[Fe(bpp)_2]^{2+}$ has been widely studied with a solvent free phase undergoing an abrupt SCO at 261 K with a 4 K hysteresis loop. A nitromethane solvated LS polymorph was also obtained through crystallization at 240 K.[56] The complex ions form a terpyridine embrace motif with face-face π-π interactions and edge to face C-H···π interactions. The complex ions pack into four-fold layers parallel to the (001) crystal plane with the anions occupying the cavities in the layers. Introduction of halide functionality at the pyrazolyl 4 position has been shown to lead to abrupt transitions, with packing in the terpyridine embrace motif showing edge-to-face C-X···π (X= Cl, Br or H) contacts between cations. The 2,6-di(4-iodopyrazol-1-yl)pyridine iron complex salts does not pack into a terpyridine embrace and are low spin at all temperature ranges measured; the failure to pack to into the terpyridine embrace was attributed to the steric bulk of the iodo substituent.[57]

Different distortion parameters have been used to study the structure and behaviour of these solid $[Fe(bpp)_2]^{2+}$ complexes (figure 10). The octahedral volume V_{oh} is calculated by summing all the Fe-N bond lengths and is typically 9-10 Å^3 for LS and 11-12 Å^3 for HS complexes. There are two octahedral distortion parameters $\sum$ and Θ. $\sum$ is the rhombic distortion parameter obtained by the summation of all 12 *cis* N-Fe-N bond angles from the ideal 90° angle. Θ is the trigonal distortion parameter obtained by the summation of all 24 dihedral angles between *cis* N donors on the opposite triangular faces. The value of Θ tends to be much larger for HS configurations.

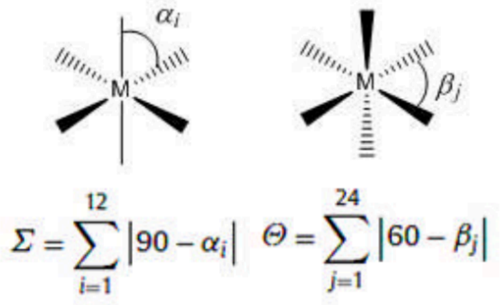

$$\Sigma = \sum_{i=1}^{12} |90 - \alpha_i| \quad \Theta = \sum_{j=1}^{24} |60 - \beta_j|$$

Figure 10 Rhombic and trigonal distortion parameters for $[Fe(bpp)_2]^{2+}$ derivatives

Another important parameter is the ligand bite angle (α) which is an average of all the $N_{pyridyl}$- Fe-$N_{pyrazolyl}$ bite angles. The HS state has longer bond lengths and thus smaller bite angles. The importance of the ligand bite angle has been shown in complexes of the related ligand family 2,4-dipyrazolyl-1,3,5-triazine (bpt). All studied salts of $[Fe(bpt)_2]^{2+}$ are HS both in the solid state and in solution, which has been attributed to a small narrowing of the bite angle relative to bpp complexes.[58] Steric requirements may also greatly affect the spin state in both the solid state and solution, with sterically demanding coordination spheres generally resulting in HS complexes.[59]

The electronic effects of ligand substituents on the spin state have also been studied in $[Fe(bpp)_2]^{2+}$ complexes with clear trends being observed. The study was carried out in solution using Evans method so as to remove lattice effects, thus the value of $T_{1/2}$ would primarily be affected by the pyridyl and pyrazolyl substituents. Functionality was introduced at the pyridyl 4 position and the pyrazolyl 4′ position. It is worth noting that the pyridyl 4 position is *para* to that heterocyclic N donor while the pyrazolyl 4′ position is *meta* to its N-donor atom. Introduction of substituents at other pyridyl and pyrazolyl positions may have greater steric effects and trap the spin state.[26] Hammett parameters (σ_p for pyridyl and σ_m for pyrazolyl) were used to quantify the electron-withdrawing and donating capabilities of the substituents (figure 11).[60]

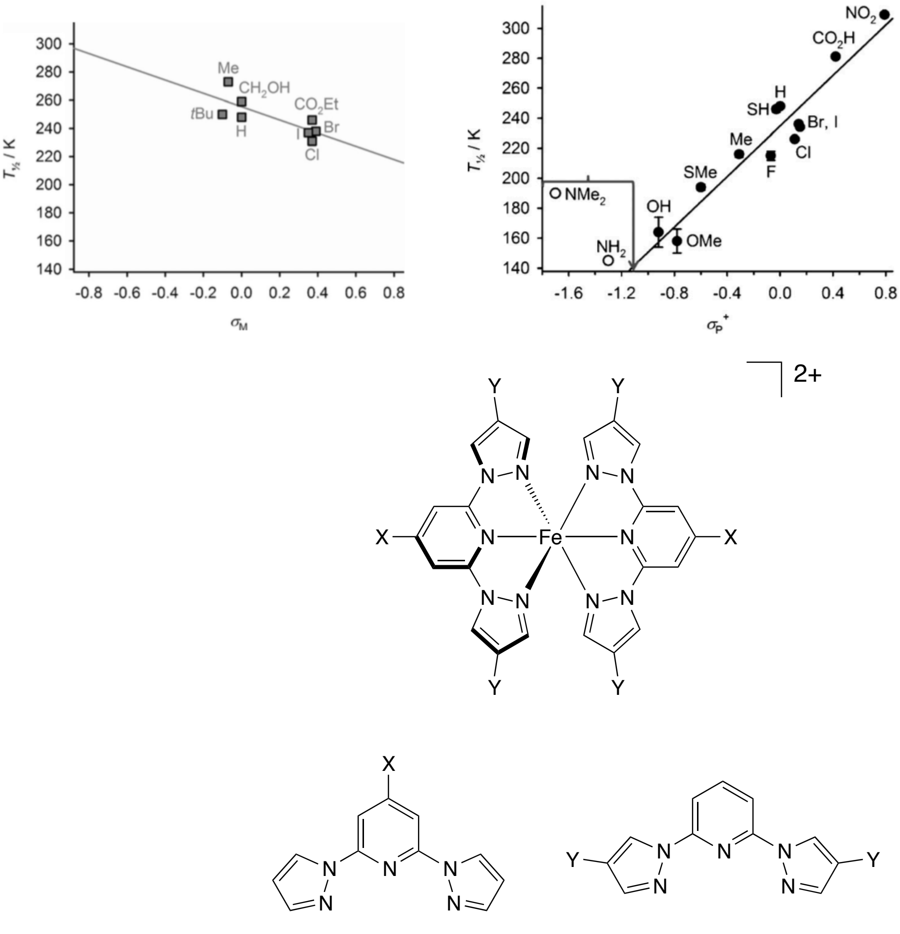

X= H,
Me, CH_2SCN, CO_2H,
F, Cl, Br, I,
NH_2, NMe_2, NO_2,
OH, OMe,
SH, SSbpp, SMe, SOMe,
SO_2Me

X= H,
Me, CH_2OH, tBu, CO_2Et,
Cl, Br, I

Figure 11 Hammett parameter vs $T_{1/2}$ plots of complexes used in study by Halcrow *et al.*

When the adjusted Hammett parameter σ_p^+ was used to factor in conjugation effects on the donor N due to the substituents a more linear correlation was observed, thus there is an Fe-N π-bonding contribution to the trend. It was shown that electron withdrawing pyridyl substituents stabilised the LS state as did electron donating pyrazolyl substituents, both of them increasing $T_{1/2}$. Conversely electron donating pyridyl substituents and electron withdrawing pyrazolyl substituents stabilised the HS state decreasing $T_{1/2}$.[51] Electron withdrawing pyridyl substituents decrease the energy of the pyridyl π^* anti-bonding orbital and thus increase the magnitude of Fe-N π-backbonding and stabilise the LS state. In contrast to this electron withdrawing pyrazolyl substituents stabilise the HS state, this can be explained by the inductive effect causing a decrease in ligand to metal σ donation and a decreased ligand field, as substituents at the pyrazolyl 4 position are out of conjugation to the donor N atom. The fact that there is 2:1 ratio of pyrazolyl donors to pyridyl donors in the molecule results in a greater effect from the pyrazolyl substituents on the spin state.

1.8 Electronic Effects of Ligand Substituents

Other similar studies have been carried out on ligand effects on spin state. Prat *et al* have studied Fe(II) complexes of Pytacn ligands (pytacn = 1-[(4-R'-6-R-2-pyridyl)methyl]-4,7- dimethyl-1,4,7-triazacyclononane) where functionality was introduced at the R and R' positions (figure 12).[61]

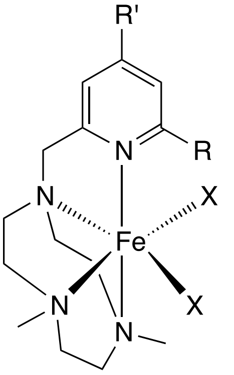

X= CF_3SO_3 or CH_3CN
R= H, Cl, F, Me
R'= H, NMe_2, OMe, Me, Cl, CO_2Et, NO_2

Figure 12 $[Fe(Pytacn)_2]^{2+}$ complexes investigate by Corona *et al*.

R' substituents were used to investigate their electronic effects on the pyridyl donor whilst R substituents were used to investigate the steric effects. In agreement with previous studies introduction of bulkier substituents at the R position produced high spin complexes. In agreement with the study carried out by Halcrow *et al* electron withdrawing *para* pyridyl substituents were found to stabilise the LS state. This is indicative of the greater π-acceptor and weaker σ-donor character of the pyridyl donor functionalised with an electron withdrawing group. Another similar study was carried out by Nakano *et al* investigating dinuclear Fe(II) complexes.[62] A pyrazolato bipyridine-bridged Fe(II) system was employed with functionality introduced through axially coordinated pyridines with the coordination sphere completed with cyanate ligands (figure 13). Functionality was introduced at the pyridyl 3 and 4 positions while two different cyanates were compared, $NCBH_3^-$ and NCS^-. It was found that complexes of $NCBH_3^-$ had a higher $T_{1/2}$ value than the corresponding analogues of NCS^-, this is consistent with $NCBH_3^-$ exerting a stronger ligand field.[63] For a given cyanate it was found that with increasing the electron withdrawing capabilities of the pyridyl substituent led to an increase of $T_{1/2}$. Strong linear correlations were observed with the plot of $T_{1/2}$ vs the appropriate Hammett parameter with R= 0.94 for NCS^- and 0.83 for $NCBH_3^-$. The apparent trend for pyridyl donors is that electron withdrawing groups decrease the magnitude of σ donation to the Fe(II) ion whilst also increasing the π-acceptor properties of pyridine and stabilising the low spin state. Electron donating pyridyl groups make the pyridine a greater σ-donor and thus produce a smaller ligand field and HS complexes. This also agree with Halcrow *et al* and Prat *et al*.

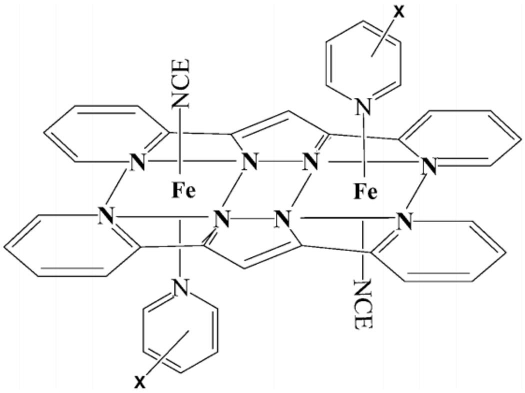

Figure 13 [{Fe(NCE)(X-py}$_2$(μ-bpypz)$_2$] where NCE= NCS or $NCBH_3$ and X= H, Me, NMe_2, Cl, Br.[63]

Interestingly electron withdrawing groups have also been shown to stabilise the HS state in some complexes.[64,65] Lin *et al* studied steric and electronic effects on the spin state of tetrahedral Fe(II) phosphoraminimato complexes (figure 14), bulkier groups on the ligand were again found to produce high spin complexes.[65] *Para* substituted electron donating groups on the triaryl phosphoraminimato were found to increase $T_{1/2}$ and stabilise the LS state, this in contrast with many six-coordinate Fe(II) SCO complexes.[66] Electron donating substituents increase the σ-donating capabilities of the phosphoraminimato ligand through the inductive effect, this increases the energy of the e* orbital set stabilising the LS state.

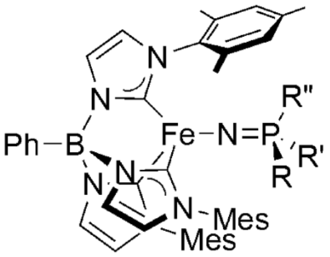

Figure 14 [(Fe-N=P(R)$_3$)(PhB(MesIm)$_3$] where R= p-XC$_6$H$_4$ (X= H, CF$_3$, Me and OMe).

The electronic effects of substituents have been explored in dinuclear Fe(II) diiminoquinonoid complexes (figure 15).[64] Electron withdrawing halide substituents were employed and it was found that the more electronegative the substituent the more it stabilised the HS state decreasing $T_{1/2}$. A linear correlation of R= 0.93 between $T_{1/2}$ and the electronegativity on the Pauling scale (χ_p) was observed. This would indicate that the ligand field is predominantly influenced by the inductive effects, the more electronegative the substituent the lower the magnitude of σ and π-donation and thus the weaker the ligand field. It is interesting that electron-withdrawing groups may have different effects on the spin state depending on the ligand used. Thus more work is required to understand the electronic effects of ligands on spin state and for the design of tuneable SCO materials.

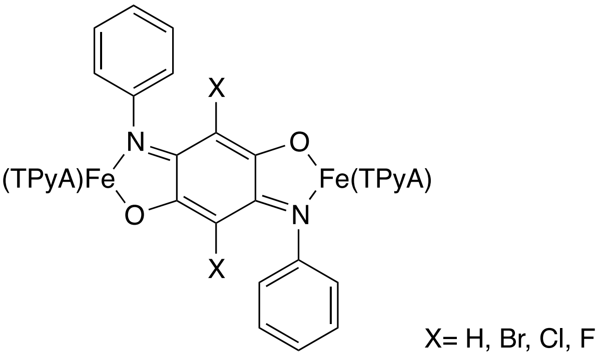

Figure 15 [(TPyA)$_2$Fe$_2$(^{X}L)]$^{2+}$ (TPyA= tris(2-pyridylmethyl)amine) (L= doubly deprotonated 3,6-disubstituted 2,5-dianilino 1,4-benzoquinone).

1.9 Project Aims

SCO active materials with practical application require control of the temperature of transition and the degree of cooperativity associated with the transition. Both parameters are effected by the packing of the lattice and the electronic effects of ligand substituents, and are ongoing areas of research. Packing effects have been well studied with the observation of sterically demanding ligand spheres resulting in HS complexes. Electronic effects of substituents of similar size primarily effect the temperature of transition, thus they are vital for tuning the $T_{1/2}$ of SCO materials. With regards to $[Fe(bpp)_2][X]_2$ salts clear trends have emerged, however further work is required to obtain a comprehensive understating of the ligand substituent effects. The aim of this project is to continue the study carried out by Halcrow *et al* on the electronic effects of substituents on the spin state of $[Fe(bpp)_2]^{2+}$ complexes. Two new bpp ligand families (figure 16) have been synthesised and characterised, containing both pyridyl and pyrazolyl substituents. The study will focus on both the solution phase and solid state SCO behaviour of the complexes with the aim of determining if the substituents effects on SCO occur additively (section 1.7). Another aim is to reduce **L^1** to give a bpp ligand **L8** with a primary amine to allow for further chemistry. It was thought this could be a precursor to new heterometallic multi-functional SCO complexes although that was not achieved during the duration of this project.

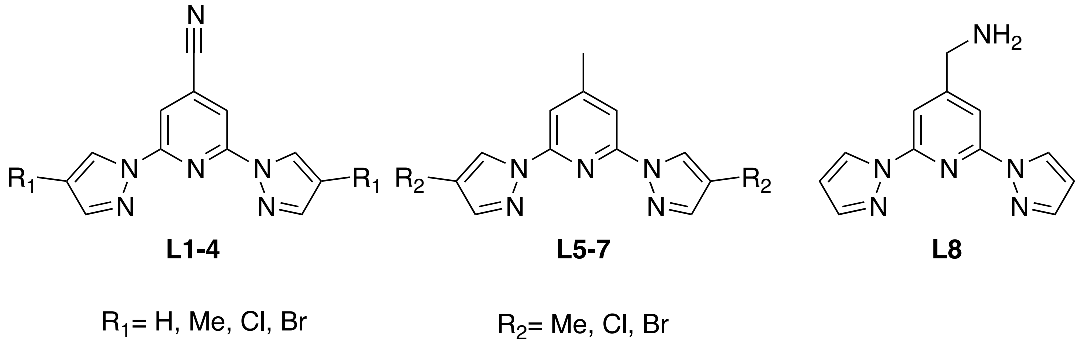

Figure 16 Target Ligands.

Chapter Two: Results and Discussion

2.1 Ligand Syntheses

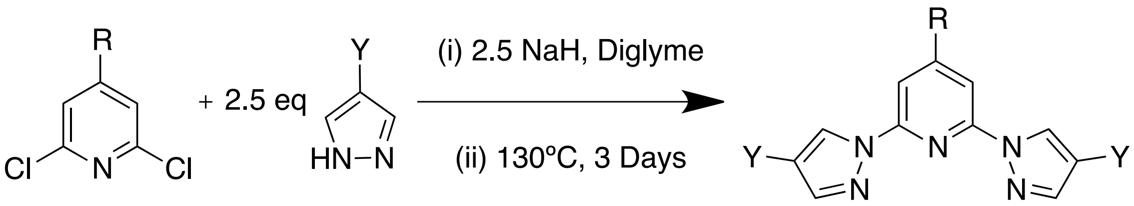

Scheme 1 Synthesis of 1-bpp ligands.

Synthesis of the new 1-bbp ligands followed a literature procedure whereby an excess of sodium hydride and pyrazole are reacted with a 2,6-dihalogenated pyridine (scheme 1).[67] Nucleophilic coupling of pyrazolide anions generated *in situ* with the 2,6-dihalogenated pyridine, in diglyme was used to synthesize the functionalized bpp ligands.[48] Yields between 40-70 % were typically obtained after three days reflux at 130°C, with a greater excess of sodium hydride and pyrazole increasing the yield. The products were precipitated as white powders by the addition of excess water to the solution, followed by filtration and washing with water and hexane. 2,6-Bis(4-methyl-1H-pyrazol-1-yl)-4-methylpyridine **L5** was not washed with hexane as the ligand was found to be soluble in hexane. Ligands were typically crystallised from DCM. 2,6-Di(1*H*-pyrazol-1-yl)isonicotinonitrile **L1** crystallized solvent free in the body centered I2/a space group. The pyrazolyl rings are in a *trans-trans* configuration to prevent a steric clash between pyridyl and pyrazolyl H atoms, as is usually observed for bpp ligands.[57,68] The ligand molecules pack in alternating sheets (figure 17).

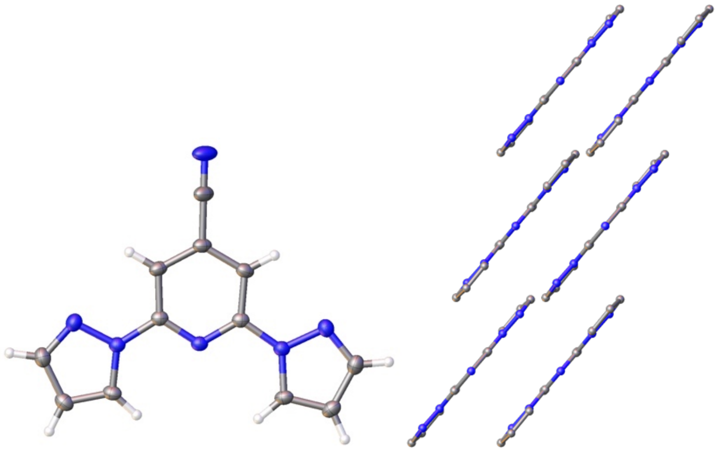

Figure 17 crystal structure (left) and packing (right) of L^1 at 120 K

The presence of 2-chloro-6-pyrazolylpyridine products was observed by mass spectrometry, and then were isolated on occasion. Attack by the second pyrazolide anion is much slower than the first explaining why this was observed.[67] Ligands derived from 2,6-dichloroisonicotinonitrile showed increased reactivity at the nitrile carbon. Purification of 2,6-bis(4-methyl-1*H*-pyrazol-1-yl)isonicotinonitrile by silica gel chromatography led to the isolation of the hydrated primary amide product **L^{2a}**. Nitriles are typically converted to amides by acid or base catalysis.[69] Previous studies have shown that nitrile hydration rates increase with presence of electron withdrawing groups adjacent to the carbon making it more prone to nucleophilic attack.[69] The acidic silica gel may have catalyzed the reaction. These amide ligands were found to be less soluble than the corresponding nitriles, and typically required dimethylsulfoxide as a solvent. The decreased solubility can be explained by the packing of the solid as **L^{2a}** shows extensive hydrogen bonding between the amide, carbonyl and pyrazolyl lone pairs between adjacent molecules. Each amide nitrogen is involved in two hydrogen bonds one to a carbonyl oxygen and one to a pyrazolyl nitrogen (figure 18). N_{amide}-H-O distances were found to 2.84(14) Å while N_{amide}-H-$N_{pyrazolyl}$ were found to be 2.96(15) Å in length. These are typical values for moderately strong hydrogen bonds.[70]

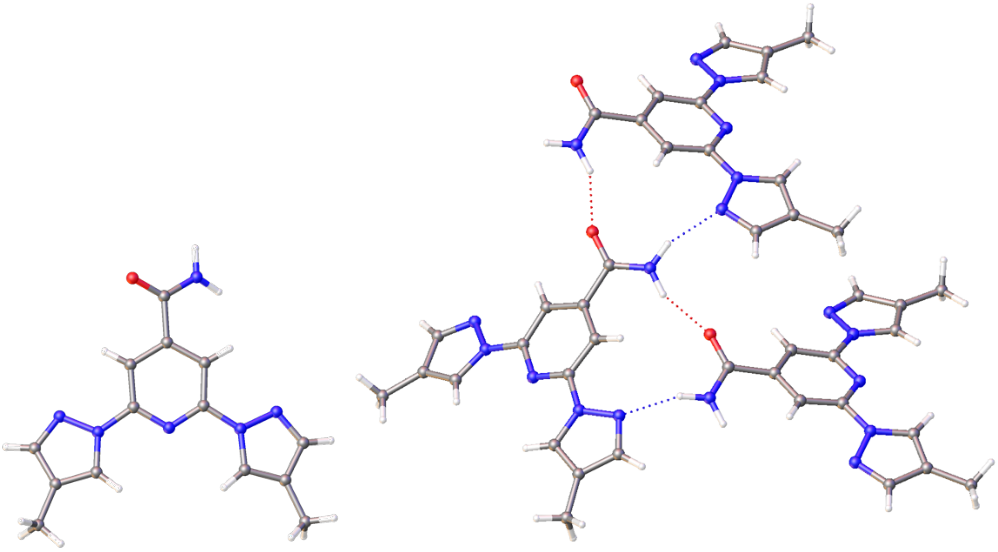

Figure 18 crystal structure and hydrogen bonding network of L^{2a} at 120 K

The syntheses of ligands derived from 2,6-dichloropicoline did not require purification steps and proceeded in higher yields. 2,6-Bis(4-bromo-1H-pyrazol-yl)-4-methylpyrdine crystallized in the primitive $P2_12_12_1$ space group with *trans-trans* pyrazolyl ring conformations (figure 19). The molecules packed in alternating zigzagging sheets featuring π-π stacking between layers.

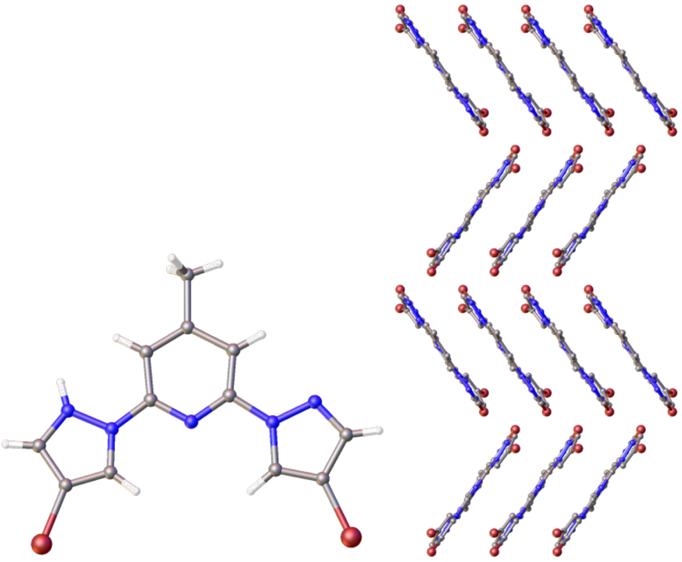

Figure 19 crystal structure (left) and packing diagram (right) of L^7 at 150 K.

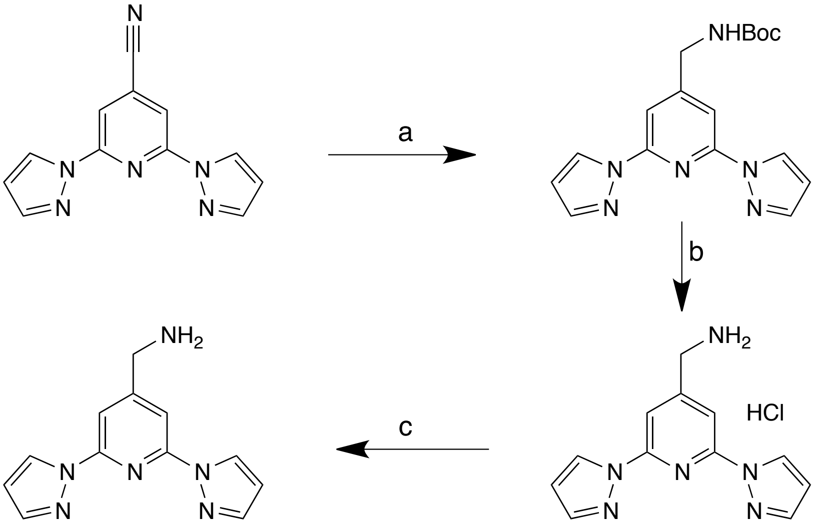

Scheme 2 Synthesis of L^8 a) 3.5eq Boc_2O, 0.1 eq $NiCl_2 \cdot 6H_2O$, 7.3 eq $NaBH_4$, 5eq diethylenetriamine, MeOH (anhy). b) acetyl chloride. c) MeOH (anhy), Na_2CO_3, H_2O, $CHCl_3$

L^8 was synthesised by the catalytic reduction of **L^1** using sodium borohydride and a nickel chloride catalyst following a literature procedure (scheme 2).[71] Excess di-tert-butyl dicarbonate was used, the resultant Boc protecting group was subsequently removed by hydrolysis in methanolic hydrochloric acid. The salt product was then neutralised using sodium bicarbonate. All steps required the use of anhydrous solvents to reduce **L**^{1} to avoid formation of the corresponding amide. The amide product was detected by mass spectrometry with an $[M+Na]^+$ peak of 277.0808 m/z with a calculated m/z of 277.0814. The presence of amide was also readily detectable by its insolubility in methanol and most organic solvents.

2.2 Iron(II) Complexes of 2,6-di(1*H*-pyrazol-1-yl)pyridine Analogues

Fe(II) complexes of 2,6-di(1H-pyrazol-1-yl) pyridine have been studied for their tunable SCO behavior. Bpp is versatile terpyridine analogue which is a widely studied ligand for SCO and luminescence.[48,72] Bpp is a weaker σ-donor than terpyridine and a weaker π-acceptor due to the higher energy of the pyrazolyl rings relative to the pyridyl rings. Bpp ligands therefore generate smaller ligand fields than terpyridine ligands, the smaller ligand field being of the correct magnitude to allow for SCO in Fe(II) complexes. Two equivalents of the planar ligand bind meridionally to the Fe(II) ion. The synthesis of $[Fe(bpp)_2][X^-]_2$ salts is straightforward with reaction of two equivalents of ligand with the desired Fe(II) salt with either nitromethane of acetonitrile as the solvent (scheme 3).

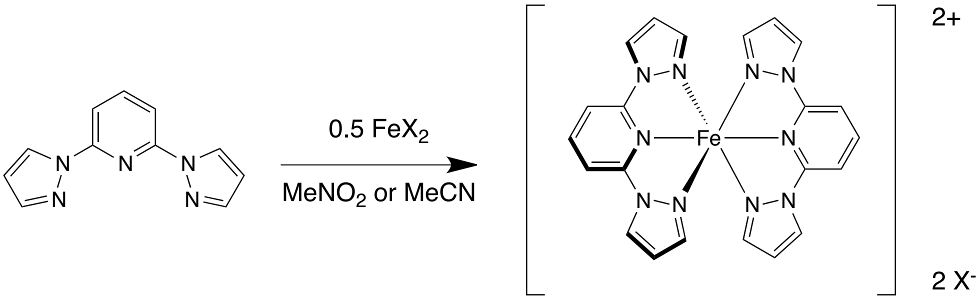

Scheme 3 Synthesis of $[Fe(bpp)_2][X]_2$ salts.

Colour changes were instantly observed upon addition of the Fe(II) salt to the solution containing the ligand. Reactions were typically complete within 30 minutes, which was mainly influenced by the solubility of the ligand and Fe(II) salt. Crystals were grown by slow diffusion with diethyl ether or diisopropyl ether. If crystals were not obtained through diffusion, powders were readily precipitated by addition of diethyl ether to filtered solutions of the complex salts. The aim of this work is to investigate the electron effects of ligand substituents on the spin state in two families of $[Fe(bpp)_2][X]_2$ salts in both solution and solid phases. Salts were analyzed by diamagnetic and paramagnetic ^{1}H-NMR spectroscopy, Evan's method, SQUID magnetometry, X-ray diffraction and elemental analysis.

2.3 Electron Effects of Substituents on Spin State

2.3.1 Magnetic Susceptibility Measurements in Solution

The solution phase SCO behavior of complex salts from both ligand families has been studied with a particular interest in the electronic effects of the substituents. This was investigate by Evans method, acetone and acetonitrile were the solvents used with TMS as the reference. The van't Hoff equation has been used to obtain values for the enthalpy (ΔH) and entropy (ΔS) of transition and $T_{1/2}$ from the Evan's method data.[47]

$$(1)\ \ \Delta G = \Delta H - T\Delta S$$

$$(2)\ \ \Delta G = -RT \ln K_{eq}$$

$$(3)\ \ \ln K = T\Delta S - \Delta H / RT$$

Plots of ln(K) (where K is the equilibrium constant for the two states) vs 1/T give $\Delta S/R$ and $-\Delta H/R$ as the intercept and slope respectively. As the gas constant R is known both the entropy and enthalpy of transition maybe calculated. At the temperature of transition the populations of the HS and LS states is equal so the equilibrium constant K=1. Substituting K=1 into equation 3 allows for the calculation of $T_{1/2}$.

The electronic effects on $T_{1/2}$ have been studied. The results have been compared within each ligand family and to overall studies carried out by Halcrow *et al*. The Hammett constants σ_p^+ for the nitrile and methyl group are 0.66 and -0.17 respectively.[60] From these values it is apparent that the nitrile is strongly electron-withdrawing whilst the methyl group is moderately electron donating. Electron withdrawing groups in the pyridyl 4 position decrease the energy of the π^* antibonding orbital and increase π-back donation, stabilizing the LS state. Electron donating groups on the pyridyl rings reduce the magnitude of π-back bonding and thus produce a smaller ligand field and stabilize the HS state. These effects were visible by the colour of the solutions of the complex salts, with complex salts of the isonicotinonitrile series being red-orange in solution whilst the corresponding 4-methylpyridine bpp complex salts gave yellow solutions indicative of higher HS state populations in solution. The σ_M values for H, Me, Cl and Br are 0, -0.07, 0.37 and 0.39 respectively.

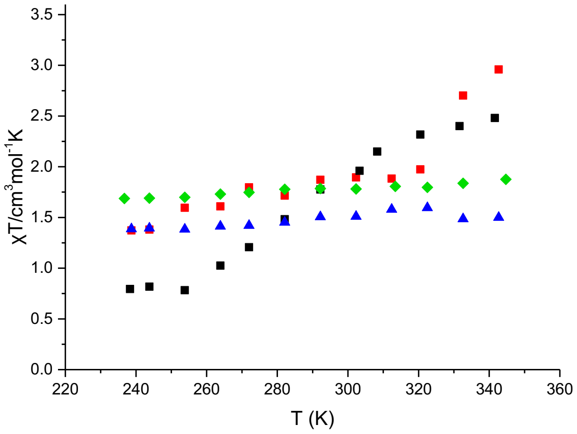

Figure 20 Variable temperature magnetic susceptibility curves of 1a (black), 2 (red), 3 (blue) and 4 (green). solubilized complex di-tetrafluoroborate salts measured in acetone-d_6 or acetonitrile-d_3

Magnetic susceptibility measurements of the nitrile ligand family of iron(II) complex salts show the parent salt **1a** undergoing SCO with a $T_{1/2}$ of 271 K, while **2** has a $T_{1/2}$ of 291 K (figure 20). These two values are in agreement with the Hammett constants for the hydrogen and the methyl group. Methyl bearing pyrazolyl complexes are expected to have higher values of $T_{1/2}$ than the respective hydrogen bearing complex.[51] The magnetic susceptibility of **3** and **4** do not decrease drastically and are intermediate between that of fully HS and LS making calculation of $T_{1/2}$ inaccurate. It is likely there are different species in solution and thus the Evans method data may not be reflective of the spin state. This was investigated further by NMR spectroscopy (section 2.3.2).

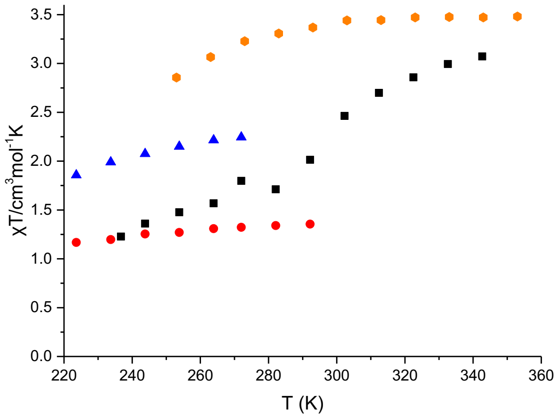

Figure 21 Magnetic susceptibility plots of 5a (black), 6 (red), 7 (blue) and $[Fe(bpp^{Me,H})_2][BF_4]_2$ (orange).

Salts of $[Fe(bpp^{Me, H})_2]^{2+}$ have previously been studied and magnetic measurement data was obtained from the reference.[53] $[Fe(bpp^{Me,H})_2][BF_4]_2$ has a $T_{1/2}$ of 216 K in solution.[51] Salt **5a**, the 4-methylpyrazolyl analogue of $[Fe(bpp^{Me,H})_2][BF_4]_2$, has a $T_{1/2}$ value of 259 K in solution (figure 21), this difference is indicative of the electron donating character of the methyl groups on the pyrazole. As there are four pyrazolyl donors in the Fe(II) complex, this increase in $T_{1/2}$ is accentuated. Interestingly the 4-halopyrazolyl complex salts show a magnetic susceptibility intermediate between that of HS and LS similar to that of the isonicotinonitrile series. The $T_{1/2}$ of **1a** is in agreement with the previous study, including it in the graph of σ_p^+ vs $T_{1/2}$ gives an R^2 value of 0.914 (figure 22).

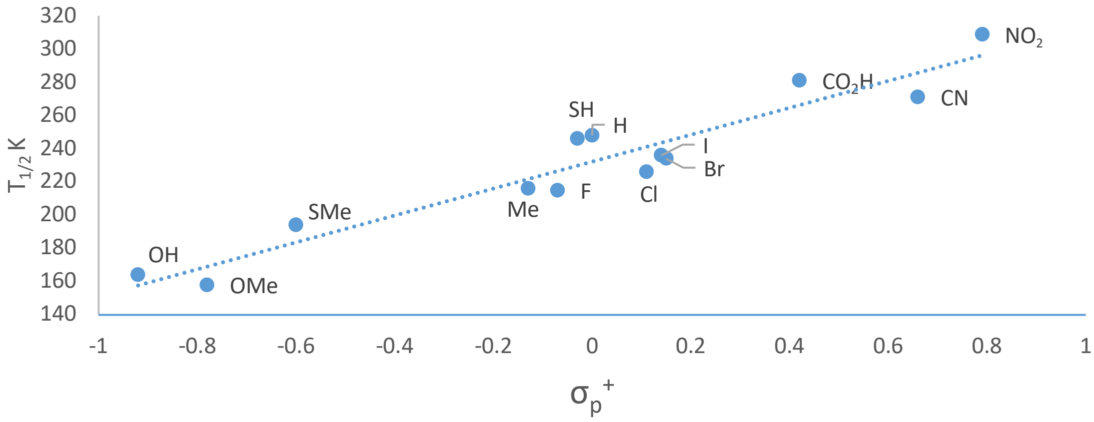

Figure 22 Plot of $T_{1/2}$ vs σ_p^+ for 4-pyridyl functionalised $[Fe(bpp)_2]^{2+}$ salts including 1a.

2.3.2 Paramagnetic ^1H-NMR Spectrscopy

To probe the nature of the species in solution paramagnetic NMR spectroscopy was carried out on all of the salts. Protons on a ligand coordinated to a HS Fe(II) ion are expected to have a chemical shift in the range of 20-200 ppm.[73] The 4-halopyrazolyl $[Fe(bpp)_2]^{2+}$ complex salts show chemical shifts for free ligand, with less intense peaks for the coordinated ligands. The paramagnetic ^1H-NMR spectrum of **7** shows many peaks in the diamagnetic region, with those over 40 ppm being of much lower intensity (figure 23).

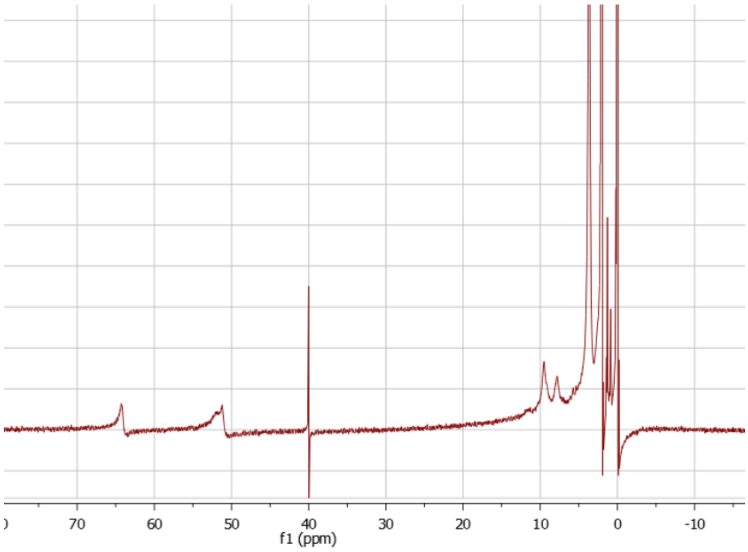

Figure 23 Paramagnetic ^{1}H-NMR spectrum of 7 in acetone-d^6

This indicates the presence of free ligand in solution and thus some decomposition of the complexes, accounting for the anomalous magnetic moments of these complexes (section 2.3.1). The degree of decomposition is unknown and thus the concentration of the complex in solution is also unknown. As the calculations for Evans method use concentration from mass per volume of solvent, it does not factor in molar concentrations.[46] This leads to an error in calculations with the signal most likely originating from a HS paramagnetic species in solution with a small decrease in magnetic susceptibility from the complexes that have not decomposed undergoing SCO. Coordination of acetone upon loss of one ligand moiety would lead to a HS complex and would explain why the magnetic susceptibility is fairly constant.[74] This has not been observed for other 4-halopyrazolyl $[Fe(bpp)_2]^{2+}$ complex salts in solution but could be expected for the isonicotinonitrile series. The electron-withdrawing nature of the nitrile leads to the pyridine being a weaker donor in addition to the decreased σ-donation of halopyrazoles, and thus making these complexes more labile in solution.

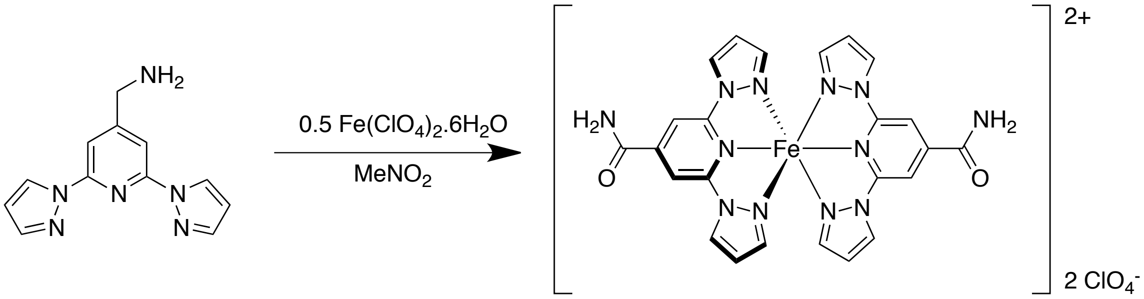

Scheme 4 Synthesis of 8.

Reaction of **L**^{8} with Fe(II) perchlorate yield crystals of **8** (scheme 4). The paramagnetic NMR spectrum of **8** (figure 24) shows only 4 proton environments in the paramagnetic region of the spectrum. The absence of a fifth signal for the methyl amine protons indicate that oxidation of amine occurred. The diamagnetic peaks originate for either free ligand or ligand bound to LS Fe(II) in solution. During the synthesis of **L**^{8} the formation of the amide was regularly observed. A possible source of the water that is oxidizing the amine could be from the hydrated Fe(II) perchlorate or water present in the nitromethane.

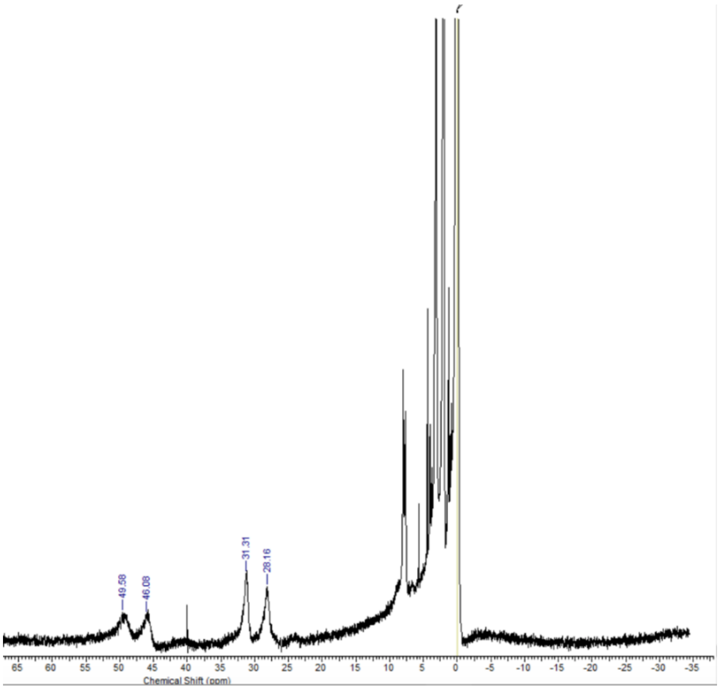

Figure 24 Paramagnetic ^{1}H-NMR spectrum of 8 in acetone-d^6.

2.4 Solid State SCO Behavior

2.4.1 Solid State Magnetic Susceptibility Measurements

The magnetic behavior of the Fe(II) complexes has been investigated by SQUID magnetometry in the temperature range of 5-375 K. Complex salts **1b,** and **1c** were found to be LS under the temperature range measured (figure 25).

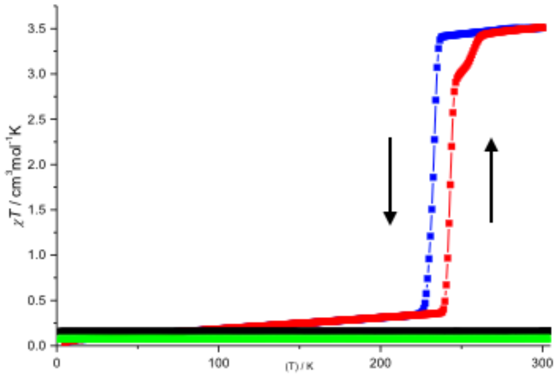

Figure 25 Magnetic susceptibility plot for 1a warming (red) and cooling (blue), 1b (black) and 1c (green).

Tetrafluoroborate salt **1a** undergoes abrupt SCO with a thermal hysteresis loop. **1a** has a warming $T_{1/2}$ of 243 K and a cooling $T_{1/2}$ of 233 K. There is also a slight change in magnetic susceptibility at 258 K, this change in magnetic susceptibility is associated with a phase change in the material. Phase changes occur for some Fe(II) SCO materials due to the difference in molecular coordinates between the HS and LS states.[13,53] The difference in $T_{1/2}$ of approximately 40 K between solid and solution phases of **1a** further highlights the profound effect of crystal packing on the thermal accessibility of SCO. **1b** is the perchlorate analogue of **1a** and would be expected to behave similarly due to the similar size and shape of the perchlorate and tetrafluoroborate anions. However, it is fully LS.[53] **1c**, the corresponding triflate salt, was also LS. The structure of these three complex salts and their spin states was further investigated by both single crystal and powder X-ray crystallography and is discussed in **section 2.4.2**.

Attempts were made to investigate packing by IR and Raman spectroscopy. However IR spectroscopy measurements of **1a** failed to detect the nitrile stretch. As the two nitrile groups in the molecule are at 180° from each other there is no change in dipole moment associated with their symmetric vibrations and thus no nitrile stretch was observed. Raman spectroscopy also failed, however Resonance Raman spectroscopy may work. Unfortunately the facilities were not available to carry out this analysis.[75]

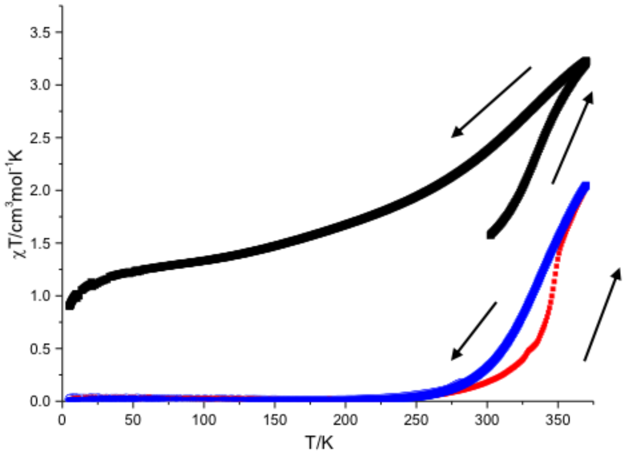

Figure 26 Magnetic susceptibility plot of 2, 1st warming (red) and cooling cycles (blue), 2nd cycle (black).

2 was found to be fully LS until 270 K where the magnetic susceptibility begins to gradually increase, however the sample never reaches fully HS in the temperature range measured (figure 26). Subsequent reruns on the same sample of **2** show that the transition is irreversible with an increase in magnetic susceptibility after each heating cycle. This behavior can be attributed to the loss of solvent from the lattice, the material is LS as a solvate and gradually converts to a phase with a higher HS population as the sample Is heated. The material likely absorbs solvent from the air whereupon it converts to a LS phase.

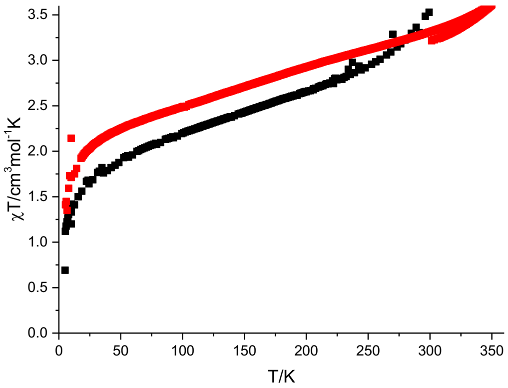

Figure 27 Magnetic susceptibility vs T plot for 3 (black) and 4 (red).

3 and **4** were both found to behave similarly with magnetic susceptibilities intermediate between that of fully HS and LS showing a gradual spin transition (figure 27). The magnetic susceptibility gradually increases upon warming reaching fully HS values at 350 K. This behavior could be due to the presence of two phases, one HS and one that undergoes a gradual SCO. Another possible explanation for this behavior is presence of solvent in the lattice, this has been investigated by X-ray crystallography and is discussed in **section 2.4.2**. The rapid decrease in magnetic susceptibility at approximately 10 K for **3** and **4** is attributed to zero-field splitting.[76] As expected the magnetic behaviour of different halogenated Fe(II) 1-bpp complexes is consistent, as the ligand field and packing effects of chloride and bromide substituents are very similar.[54]

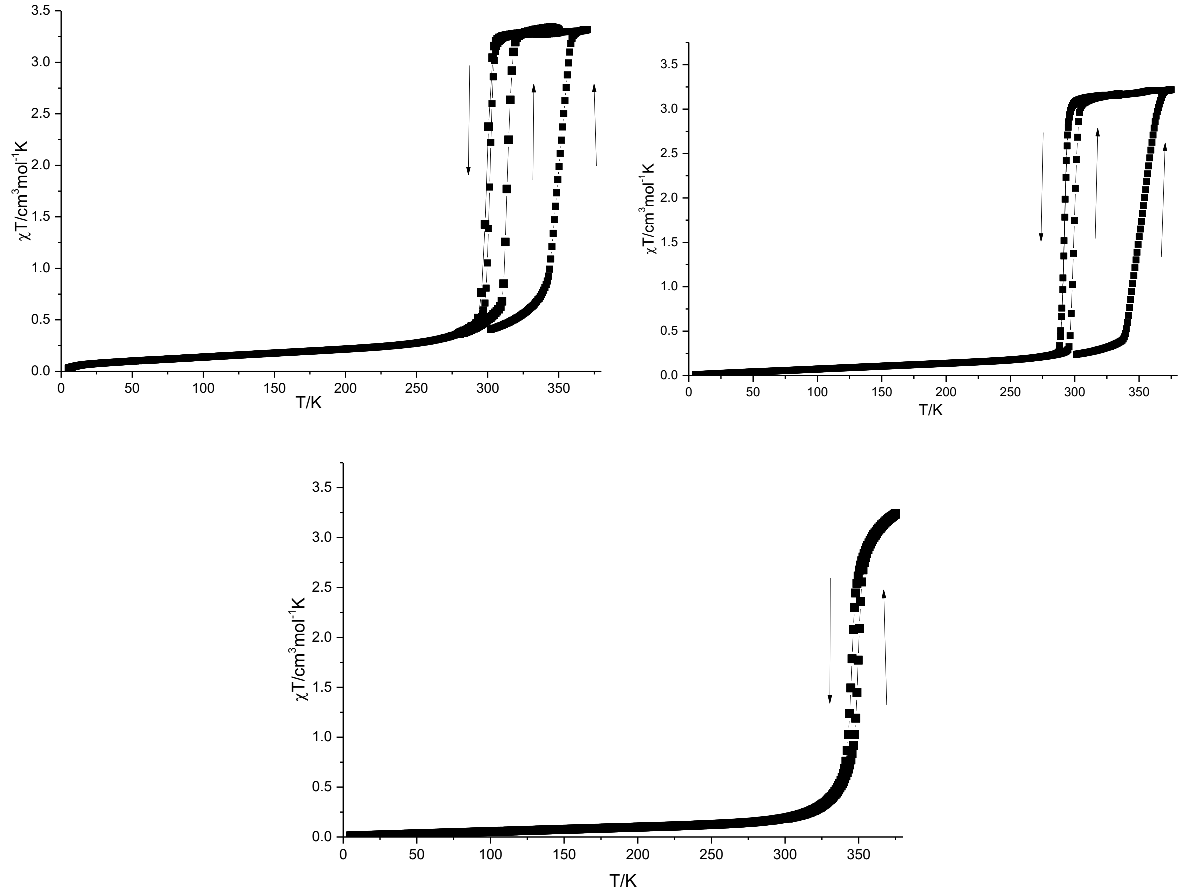

Figure 28 Magnetic susceptibility plots of 5a (top right), 5b (top left) and 5c (bottom).

The magnetic susceptibilities of salts **5a**, **5b** and **5c** have all been measured (figure 28). **5a** is LS but undergoes an abrupt transition at 350 K which is attributed to solvent loss. Upon solvent loss **5a** then undergoes abrupt SCO with an 8 K hysteresis loop at room temperature; the $T_{1/2}$ of warming is 300 K and $T_{1/2}$ of cooling is 292 K. **5b**, the perchlorate salt of **5a**, behaves very similarly and also undergoes abrupt SCO with a 15 K hysteresis loop close to room temperature upon solvent loss. **5b** has a $T_{1/2}$ of warming of 298 K and a $T_{1/2}$ of cooling of 313 K. **5c** the triflate salt also undergoes SCO with a 4 K hysteresis loop, $T_{1/2}$ of heating is 346 K and $T_{1/2}$ of cooling is 350 K. Unlike **5a** and **5b**, **5c** does not exist as a solvated polymorph prior to heating. The fact that all three salts undergo hysteretic SCO shows that **L**^{5} imparts both a ligand field and packing environment which allow for SCO provided a small enough anions is used.

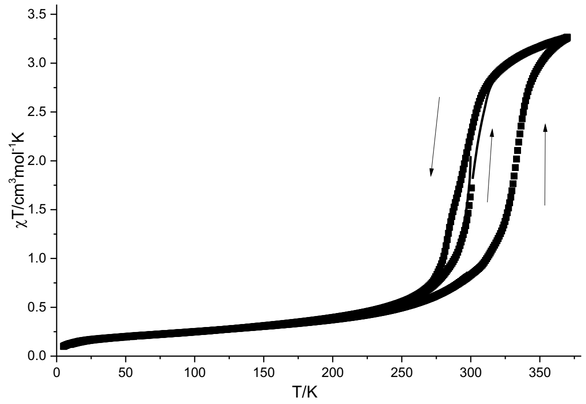

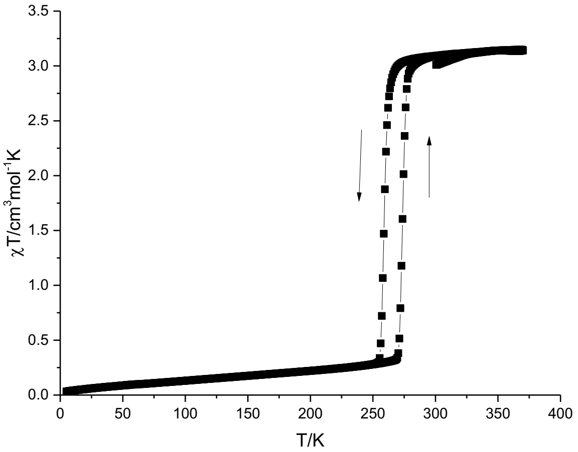

Figure 29 Magnetic susceptibility plots for 6 (top) and 7 (bottom).

Magnetic susceptibility plots of **6** and **7** show them both to undergo hysteretic SCO (figure 29). **6** is a solvate and is LS until 250 k where upon it loses solvent and transitions to HS. Solvent free **6** then undergoes SCO with a 6 K hysteresis loop and a $T_{1/2}$ of cooling of 294 K and a $T_{1/2}$ of warming of 300 K. The hysteresis loop is not in a regular shape indicating that there is a possibility of two phases being present. **7** exist as a LS nitromethane solvate until heated to 300 K where upon it loses its solvent content and transitions to a fully HS polymorph. This polymorph then undergoes reversible SCO with a 17 K hysteresis loop, the $T_{1/2}$ of warming is 275 K and the $T_{1/2}$ of cooling is 258 K.

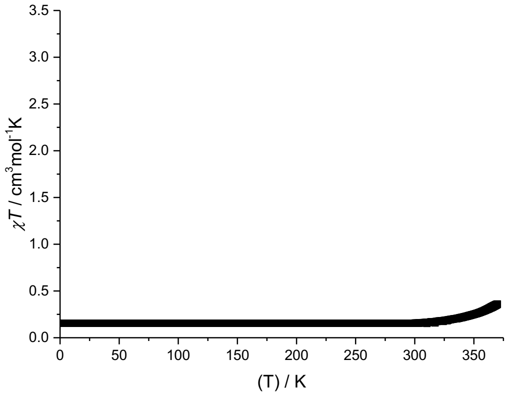

Figure 30 Magnetic susceptibility plot for 8.

8 is LS in the temperature range measured (figure 30). Amide groups are electron withdrawing when bound via the carbonyl C atom stabilizing the LS state. Neville *et al* have shown that increased hydrogen bonding may lead to the stabilization of the LS state.[77] It is possible that there is considerable hydrogen bonding throughout the material similar to $\mathbf{L^{2a}}$ preventing the geometrical changes associated with a spin transition.

2.4.2 Single Crystal and Powder Diffraction Studies

Single crystals suitable for X-ray diffraction were obtained for **1a**, **1b**, **1c**, **3**, **5b** and **7** by diffusion of either diethyl ether or diisopropyl ether into their solutions in nitromethane. Where suitable single crystals were obtained, crystalline samples of the complex salts were ground and analyzed by X-ray powder diffraction to investigate the bulk nature of the material. Powder diffraction was also used to investigate whether certain salts were isostructural in the absence of single crystal data.

Crystal structures for salts **1a**, **1b** and **1c** were all solved at 120 K, with the HS structure of **1a** obtained at 290 K as well. Crystals of **1a** are bright orange at room temperature whilst those of **1b** and **1c** are both dark red. **1a** crystallizes in the triclinic $P\bar{1}$ space group with two dications in the asymmetric unit at 120 K (figure 31). Both dications are LS by bond length and distortion parameter analysis. This is in agreement with magnetic susceptibility measurements.

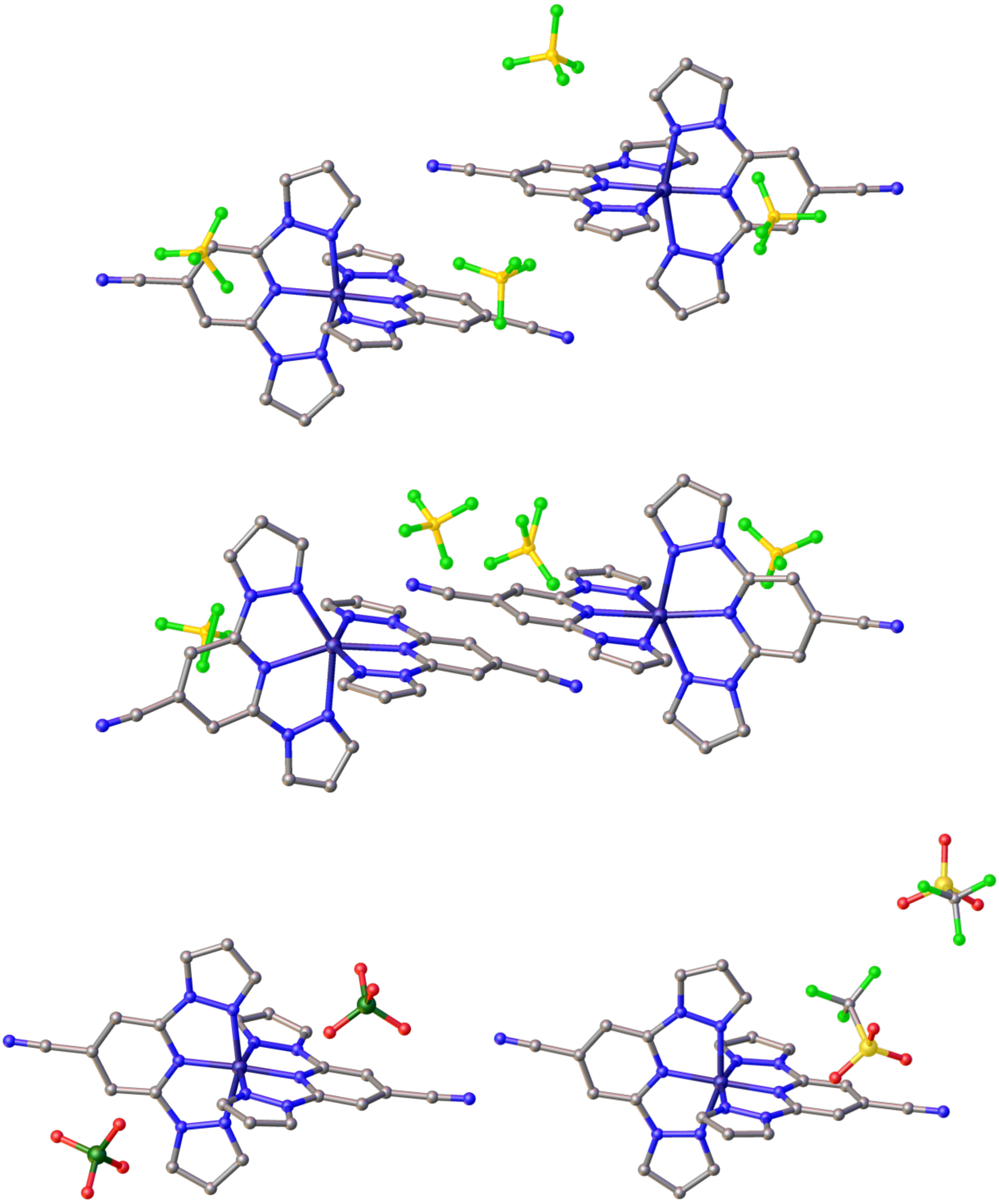

Figure 31 Crystal structures asymmetric units for 1a at 120 K (top), 1a at 290 K (middle), 1b at 120 K (bottom left), 1c at 120 K (bottom right). Hydrogens omitted for clarity.

1a, **1b** and **1c** are all LS at 120 K with **1a** being high spin at 290 K by distortion parameter analysis (table 1). HS **1a** at 290 K crystallizes in the triclinic $P2_1$ space group. The change in space group is indicative of a phase change in the material upon SCO. There are still two dications in the asymmetric unit however both are heavily distorted from ideal octahedral geometry (table 1), as is usual for Fe(II) bpp SCO materials.[21]

1b crystalizes in the triclinic $P2_1/c$ space group with one dication in the asymmetric unit (figure 31). Interestingly the unit cell parameters and space group are very different from **1a** despite the similar size of their anions. This is highlighted in the powder diffraction data for both salts. **1c**, the triflate salt of the same complex crystallizes in $P2_1/n$ space group and is LS indefinitely (figure 31). This is not as surprising as the behavior of **1b** as the triflate anion is larger and a different shape to that of the tetrafluoroborate and perchlorate. As the Fe(II) centers in the three salts are under the same ligand field, the magnetic behavior is directed by the packing and how the lattice can accommodate the HS complex. **1a** packs in a terpyridine embrace similar to previously studied $[Fe(1\text{-}bpp)_2]^{2+}$ salts which undergo hysteretic SCO.[54] The dications pack into four fold layers parallel to the 001 crystallographic plane. The packing features edge to face C-H···π contacts with distances of 3.629(10) Å and 3.684(10) Å.

Salt Cation (Temp)	Θ	Σ	V_{oh} Å^3	Av. Fe-N bond length Å	Trans Angle °	Av. Bite Angle °
1a₁ 120 K	277	84.3	9.53	1.946	173.6	80.325
1a₂ 120 K	272	82.8	9.51	1.943	178.6	80.450
1a₁ 290 K	474	153	12.15	2.173	162.2	73.117
1a₂ 290 K	468	165	11.63	2.139	159.6	73.238
1b 120 K	272	82.5	9.43	1.939	175.7	80.475
1c 120 K	281	85.6	9.52	1.945	177.6	80.164
3 120 K	280	87.4	9.49	1.943	179.1	80.168
5b 150 K	283	86.8	9.37	1.953	177.1	80.069
7₁ 150 K	273	82.8	9.46	1.916	175.4	80.455
7₂ 150 K	293	89.4	9.59	1.952	177.2	79.744

Table 1 Average bond Lengths and distortion parameters for all dications of which crystal structures were obtained.

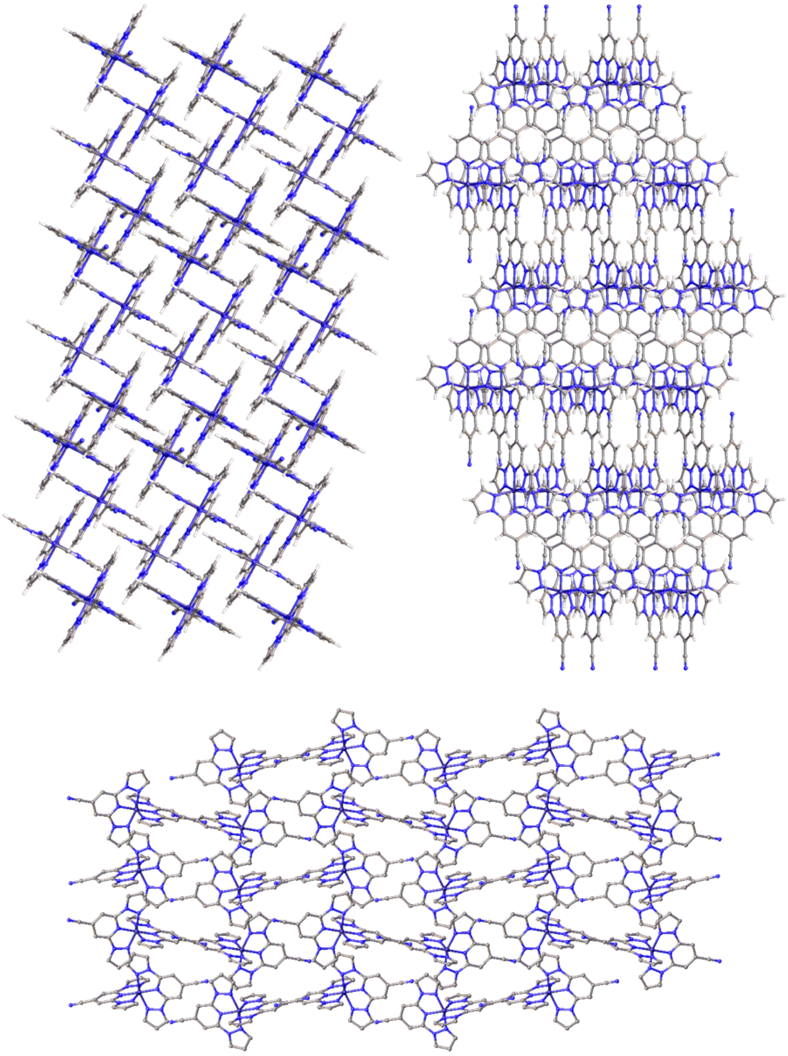

Figure 32 Packing diagrams for 1a (top left), 1b (top right) and 1c (bottom) at 120 K viewed parallel from the 001 crystallographic plane. Anions are omitted for clarity.

1b and **1c** do not pack in the terpyridine embrace which can be seen from the 001 crystallographic plane (figure 32). Powder diffraction studies of the three salts show that they are not isostructural and that the bulk samples are crystalline singular phases (figure 33).

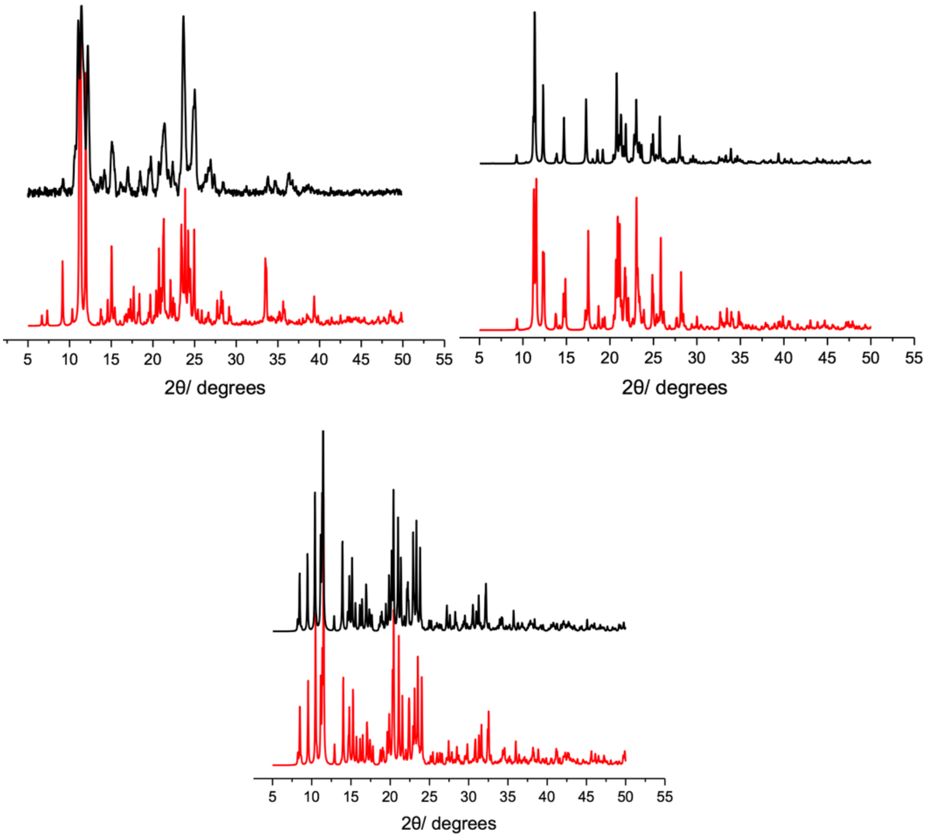

Figure 33 Experimental (black) and simulated (red) powder diffraction data for 1a (top left), 1b (top right) and 1c (bottom) at 290 K.

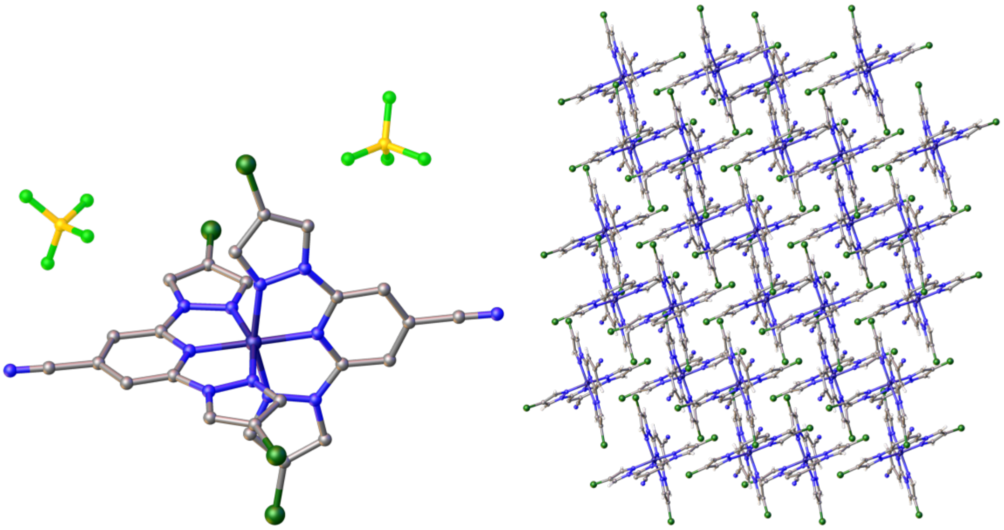

Figure 34 Crystal structure asymmetric unit of 3 at 120 K (left) and packing viewed along the 010 crystallographic plane (right).

Dark red block crystals of **3** were obtained upon ether diffusion into a nitromethane solution. **3** crystallizes as solvate with disordered nitromethane in the $P2_1/n$ space group (figure 34). **3** is LS at 120 K, in contrast to the magnetic susceptibility the complex is LS by bond length and distortion parameter analysis. The discrepancy between the crystal structure and magnetic behavior are possibly due to the presence of multiple phases in the bulk material used for the magnetic measurement. Interestingly the crystalline material packs similar to the terpyridine embrace motif with C-Cl···π contacts. Deviations from the terpyridine embrace are visible when the packing is viewed along the 010 crystallographic plane (figure 34). The powder diffraction pattern of a bulk sample of 3 upon heating shows a loss of crystallinity (figure 35). It is likely that solvent loss causes **3** to lose crystallinity and transition to a mixture of two phases one crystalline and one powder. The powder is likely HS and this would explain the magnetic susceptibility measurements of the **3**.

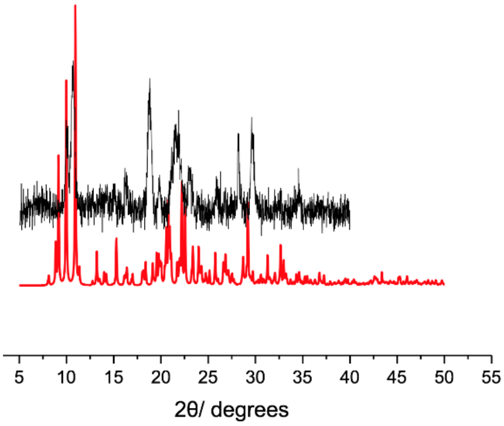

Figure 35 Experimental (black) and simulated (red) powder patterns of 3 at 290 K.

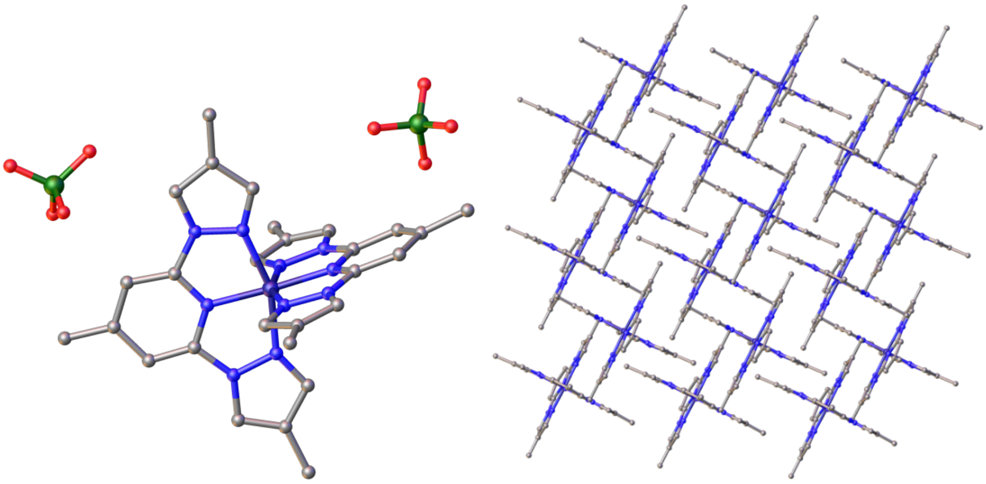

Figure 36 Crystal structure asymmetric unit of 5b (left) and packing viewed from the 001 crystallographic plane at 150 K. Anions omitted for clarity in the packing diagram.

Dark red crystals of **5b** were obtained upon diffusion of diethyl ether into a nitromethane solution of **5b**. After drying in a vacuum oven a mixture of dark red and bright orange crystals were obtained. This reflects the spin state of the sample with it undergoing SCO around room temperature. Crystals of **5a** also behaved the same however they were of poorer quality for single crystal X-ray diffraction. A crystal structure of **5b** was obtained at 150 K, but no HS structural data was obtained for the salt. The complex is LS at 150 K by distortion parameter analysis (table 1) and crystallizes in the $P\overline{1}$ space group (figure 36). Similar to **1a**, **5b** packs in a terpyridine embrace and undergoes SCO with hysteresis (figure 35). The tetrafluoroborate salt of **5a** has the same unit cell and powder diffraction pattern as **5b** indicating that they are isostructural (figure 37). The two salts undergo SCO with hysteresis at different temperatures due to the different van der waal interactions of the anions in the lattice. **5c** also undergoes SCO, however as no single crystal data was obtained for the salt, its crystal packing is unknown. The powder diffraction pattern however is different from both **5a** and **5b** showing it Is not isostructural with them.

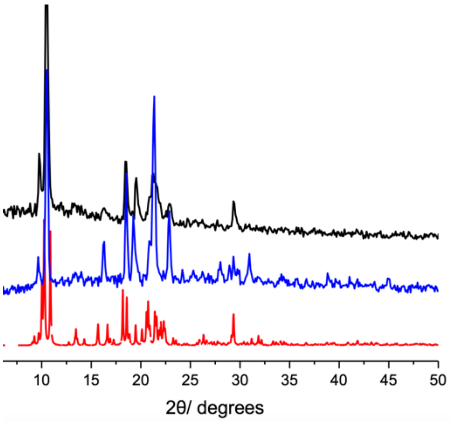

Figure 37 Powder patterns of 5a experimental (black), 5b experimental (blue) and 5b simulated (red) at 290 K.

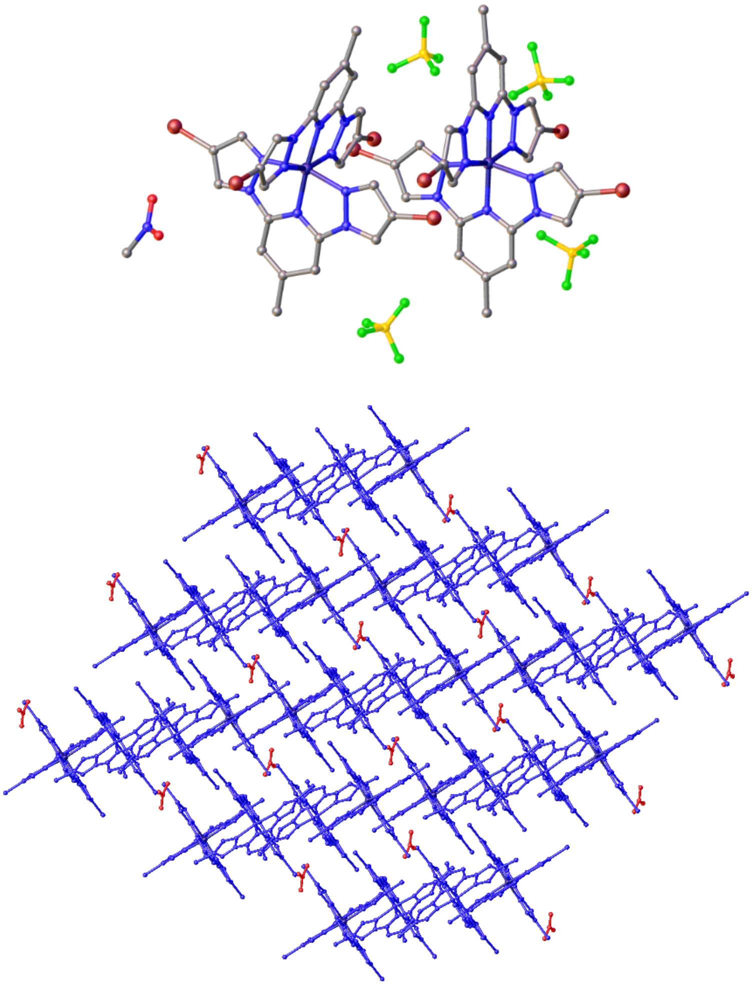

Figure 38 Crystal structure asymmetric unit of 7 (top) and packing viewed along the 001 crystallographic plane (dications in blue, MeNO$_2$ in red, anions omitted) at 120 K.

Dark red crystals of **7** where obtained upon diffusion of diethyl ether into a nitromethane solution of **7**. **7** crystalizes as a nitromethane solvate in the P$\bar{1}$ space group (figure 38). There are two dications in the asymmetric unit which are both LS at 150 K. The two dications in the asymmetric unit both feature C-Br$\cdots\pi$ interactions between the pyrazolyl rings. Similar to **1a** and **5b**, **7** packs in a terpyridine embrace with anions and solvent molecules between the four fold layers (figure 38). There are C-Br$\cdots\pi$ interactions with distances of 3.2109(15) Å and 3.2747(13) Å. Nitromethane sits in between the four-fold layers, which may prevent the molecular rearrangements required to allow for SCO. It is likely that when **7** is heated solvent loss allows the ligand arms more flexibility and thus the ability to accommodate HS Fe(II) and allow for SCO. The experimental powder pattern of **7** differs from the simulated one and shows fewer diffraction spots, this is likely due to loss of crystallinity due to solvent loss. Interestingly the experimental powder diffraction pattern of **6** is quite similar to the simulated pattern of **7**, thus it is likely they are isostructural (figure 39).

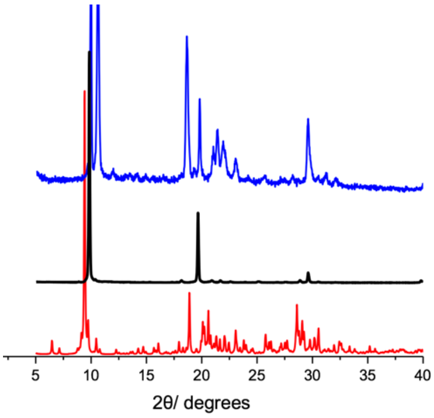

Figure 39 Powder diffraction pattern 7 simulated (red), 7 experimental (black) and 6 experiemtnal (blue) at 290 K.

2.5 Towards the Synthesis of Bimetallic SCO Coordination Polymers

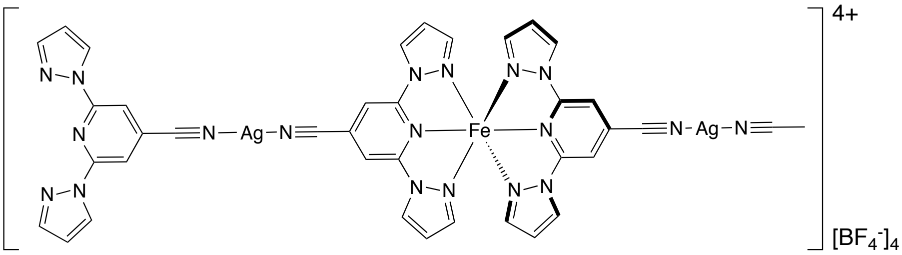

Scheme 5 Target $[Ag_2(1a)_3][BF_4]_2$ polymer.

Attempts have been made towards the synthesis of bimetallic SCO coordination polymers through coordination of the nitrile group from 2,6-di(1*H*-pyrazol-1-yl)isonicotinonitrile (scheme 5). Bimetallic bridge SCO materials are of interest due to the potential of increased cooperativity. Fe(II)-silver(I) cyanide bridged 2-dimensional SCO polymers have been studied by Munoz *et al*, where all equatorial coordination sites to the Fe(II) ion are occupied by cyanide N donors with the silver ions coordinated to the cyanide C donor with pyridyl donors completing the coordination spheres.[78]

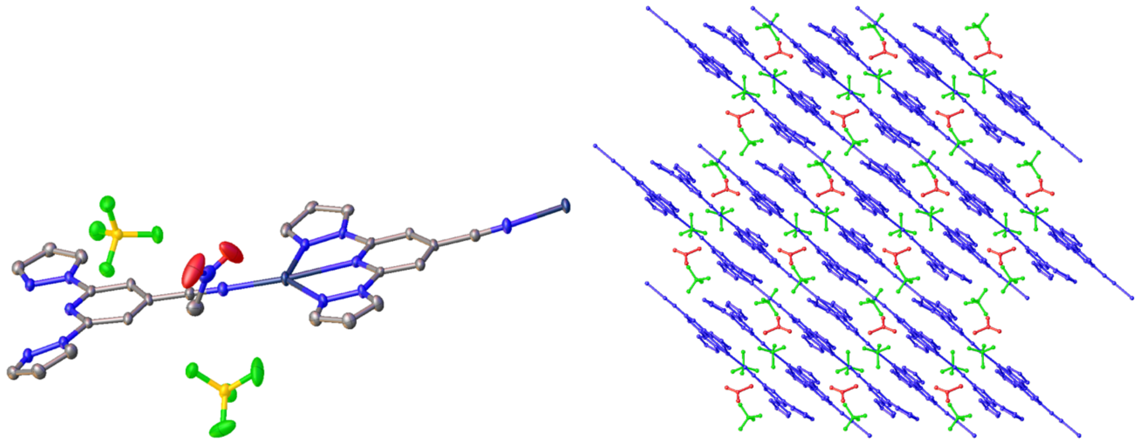

Figure 40 Crystal structure asymmetric unit (left) and packing diagram (polymer chains in blue, $MeNO_2$ in red and BF_4^- anions in green) of 9 at 120 K

Reacting **L^1** with silver(I) tetrafluoroborate gave the 1-D dimensional coordination polymer **9** where Ag(I) ions are coordinated through the pyrazolyl and pyridyl bpp donors and the nitrile group (figure 39). The polymer crystallized in the $P\bar{1}$ space group. The 1-D polymer sheets pack in layers with anions and nitromethane occupying the space between the layers (figure 40). Reaction of **1a** with silver(I) tetrafluoroborate also produced the same polymer, with silver(I) ions displacing the Fe(II) ions.

Another method of bridging cations of **1a** was through coordination of the nitrile by a cation with two vacant trans coordination sites (scheme 6). The hfac (hexa-fluoroacetylacetonato) ligand has been shown to form octahedral complexes of $M(hfac)_2(L)_2$ (where L= monodentate ligand) with both L ligands trans to each other.[79] This tendency allows for the formation of 1-dimensional linear coordination polymers.[80]

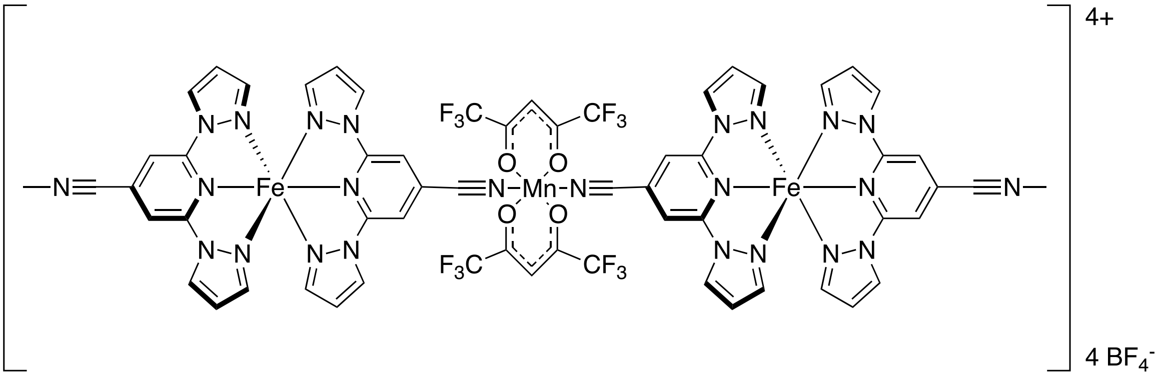

Scheme 6 Target $[Mn(hfac)_2(1a)_2]$ bimetallic polymer.

Manganese(II) hexa-fluoroacetylacetonato trihydrate was reacted with both **ligand 1** and **1a**. Both reactions yielded yellow crystals of **9**. **9** crystallized in the $P2_1/n$ space group (figure 41). The complex is 7-coordinate in a pentagonal bipyramidal geometry around the Mn(II) ion, with one molecule of **L^1** coordinated to the Mn(II) centre through the pyridyl and pyrazolyl donors. Hfac ligands have also been shown to promote the formation of seven coordinate centers.[81] Thus far the attemped synthesis of bimetallic SCO polymers using **L**^{1} have proved unsuccessful likely due to the high bonding affinity of the ligand to other metals.

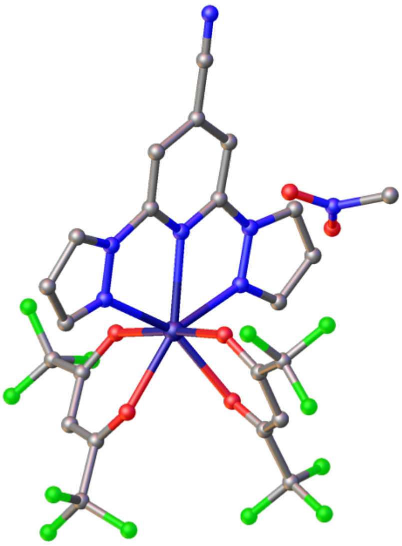

Figure 41 Crystal structure asymmetric unit of 9 at 120 K.

Conclusion:

Two 1-bbp ligand families, one containing a methyl substituent and one containing a nitrile substituent on the pyridyl 4-position have been synthesized and characterized. Fe(II) complex salts of these ligands have been successfully prepared. The electronic effects of their ligand substituents on SCO have been investigated with salts **1a**, **2**, and **5a** in agreement with previous studies. However salts **3**, **4**, **6** and **7** show an intermediate spin state in solution which is attributed to ligand dissociation. The ligands used in the synthesis of these salts all contain halogen substituents on the 4' pyrazolyl position. The solid state magnetic behaviour of the salts has been investigated with salts **1a**, **5a**, **5b**, **5c**, **6** and **7** undergoing SCO with hysteresis. Salts **5a**, **5b**, and **5c** are synthesized form the same ligand (**L5**) and thus have the same magnitude of Δ_{oct}. The difference in $T_{1/2}$ between the three salts is due to the anion choice. This is an interesting result as typically introduction of the triflate anion results in LS $[Fe(bpp)_2][X]_2$ salts, whilst tetrafluoroborate and perchlorate salts tend to behave similarly. The nature of the materials has been examined using X-ray crystallography. Most complexes have ligand field strengths that allow for SCO, however the packing of the materials greatly affect the spin state. Complexes that pack in a terpyridine embrace when viewed along the 001 crystallographic plane undergo hysteretic transitions, whilst others in the series are LS. The presence of solvent within the lattice causes the complexes to remain LS, however heating of the complexes to remove the solvent then allows for SCO. The spin states of the complexes has also been verified by distortion parameters that are well documented in the literature. Some attempts to form bimetallic SCO polymers have been made but proved unsuccessful.

Future work will expand the ligand families and investigate their complexes spin states in the solid state and solution. Further exploration of the effects of anions on the SCO behaviour of salts of $[Fe(\mathbf{L5})_2][X]_2$ is also required. Further investigation of the 4-halopyrazolyl $[Fe(bpp)_2]^{2+}$ complexes in solution is required to fully understand their magnetic susceptibility measurements.

Chapter Three: Experimental

3.1 Methods and Experimentation:

3.1.1 NMR Spectroscopy

NMR spectra were recorded on a ULTRASHIELD Advance III 300 MHz or Ascend Advance III 400 MHz (Bruker Corp.) spectrometers using automated procedures. All deuterated solvents were purchased from Sigma Aldrich, Fluorochem or Fisher and used as received.

3.1.2 Mass Spectrometry

High resolution electrospray (ES) mass spectra were recorded on an open access MicroTOF mass spectrometer (Bruker Corp.) in either positive or negative ion mode. Samples were injected directly from feed solutions diluted to 10 µg / mL and acquired over the *m/z* range 50 – 4000. Low resolution electrospray mass spectra were recorded on an open access Micromass LCT (Bruker Corp.) after passing through a short HPLC column.

3.1.3 X-ray Crystallography

Single crystal X-ray data were collected by the author. Crystals were mounted under Fomblin onto a nylon loop. Diffraction data were collected using an Agilent SuperNova diffractometer with an Atlas CCD detector using mirror monochromated Mo-*K*α (λ = 0.71073 Å) or Cu-*K*α (λ = 0.71073 Å) radiation. Data collected using synchrotron radiation was acquired at Diamond Light Source (λ = 0.6889 Å) using a Pilatus 2M detector. The structures were solved using SHELXS direct methods, and the structural model refined by full matrix least squares using SHELXL. Molecular graphics and tables of bond lengths were carried out using Olex2.

Powder diffraction patterns were collected on Bruker D2 Phaser by the author and the data was processed by Diffract. Measurement software.

3.1.4 Magnetic Susceptibility

Magnetic susceptibility measurements were carried out by Dr. Rafal Kulmaczewski and performed on a Quantum Design MPS SQUID magnetometer, in an applied field of 5000 Oe. Diamagnetic corrections were estimated from Pascal's constants, and a diamagnetic correction for the sample holder was also applied. A scan rate of 5 K per minute was used.

3.1.5 Evans Method

Variable temperature Evans method was carried out on a Bruker AVANCE 500 MHZ by Dr. Simon Barrett and Dr. Mark Howard using approximately 10 K increments over the temperature range of 238-342 K. 7.5 mg of complex were dissolved in 1 ml of CD_3CN containing tetramethylsilane as a standard for the experiment.

3.1.6 Infrared Spectroscopy

FTIR spectra were recorded using a Spectrum One spectrophotometer (PerkinElmer) fitted with diffuse reflectance probe with zinc-selenide window. IR Spectra were recorded using a globular light source through KBr beamsplitter for the range 4000-400 cm-1 using DLATGS detector with KBr window. 32 scans were recorded for each averaged spectrum with a new background recorded after each sample. IR spectra were analysed using the spectroscopy software package *OPUS* (v 6.5, Bruker Optiks GmbH).

3.1.7 Elemental Analysis

Elemental composition of samples was determined by Stephen Boyer of the Science Centre of London Metropolitan University.

3.2 Synthesis of Ligands

Synthesis of 2,6-di(1*H*-pyrazol-1-yl)isonicotinonitrile L1

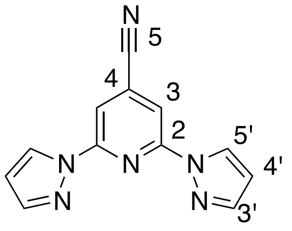

Diethylene glycol dimethyl ether (60 ml) was added to a round bottom flask with a stir bar. Sodium hydride 60% dispersion (w/w) in mineral oil (0.58 g, 14.5 mmol) was added giving a cloudy suspension. Pyrazole (0.983 g, 14.5 mmol) was added slowly, giving off bubbles of H_2 gas. The solution was stirred for 30 minutes under nitrogen. A yellow solution was obtained, 2,6-dichloroisonicotinonitrile (1.00 g, 5.78 mmol) was added to the solution. The mixture was refluxed at 130°C for 24 hrs. Giving a white suspension. The reaction mixture was allowed to cool to room temperature and quenched with excess water. The white precipitate was filtered off and washed with water and hexane. The white powder was then dried *in vacuo.*

Yield: 0.972 g, 71.2%

MP: 156-158 °C

FTIR: {CN} 2234.17 cm^{-1}

Mass Spec: $[M+H]^+$ 237.0879 m/z Calc. 237.0889 m/z

NMR: ^{1}H NMR (400 MHz, $CDCl_3$) δ 8.53 (d, J= 2.84 Hz , 2H, **3**'), δ 8.08 (s, 2H, **5’**), δ 7.81 (s, 2H, **3**) , δ 6.55 (t, J= 2.0 Hz, 2H, **4’**)

^{13}C-NMR (400 MHz, $CDCl_3$) δ 150.8 ppm (**2**), δ 143.4 ppm (**3’**), δ 127.1 ppm (**5’**), δ 125.1 (**5**) , δ 115.8 (**4**),δ 111.1 ppm (**4’**), δ 109.0 ppm (**3**)

Synthesis of 2,6-bis(4-methyl-1*H*-pyrazol-1-yl)isonicotinonitrile L2

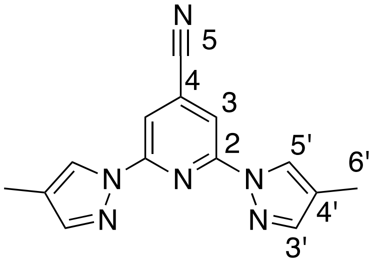

Diethylene glycol dimethyl ether (60 ml) was added to a round bottom flask with a stir bar. Sodium hydride 60% dispersion (w/w) in mineral oil (0.58 g, 14.5 mmol) was added giving a cloudy suspension. 4-methylpyrazole (1.19 ml, 14.5 mmol) was added slowly, giving off bubbles of H_2 gas. The solution was stirred for 30 minutes under nitrogen. A yellow solution was obtained, 2,6-dichloroisonicotinonitrile (1.00 g, 5.78 mmol) was added to the solution. The mixture was refluxed at 130°C for 24 hrs. Giving a yellow suspension. The reaction mixture was allowed to cool to room temperature and quenched with excess water. The white precipitate was filtered off and washed with water and hexane. The yellow powder was dried *in vacuo.* The crude product was then purified on a silica gel column (eluent ethyl acetate: hexane 7:3) isolating two products, white powder and pale yellow crystals of **L2a**.

Yield: 0.65 g, 43%

MP: 163-165 °C

FTIR: {CN} 2248.63 cm^{-1}

Mass Spec: $[M+H_3O]^+$ 283.1176 m/z Calc. 283.1302 m/z

NMR: ^{1}H-NMR: (400 MHz, $CDCl_3$) δ 8.34 (t, J= 0.98 Hz, 2H, **5'**), δ 8.12 (s, 2H, **3'**), δ 7.60 (s, 2H, **3**), δ 2.21 (s, 6H, **6'**)

^{13}C-NMR: (400 MHz, $CDCl_3$) δ 150.6 (**2**), δ 148.1 (**3'**) , δ 144.2 (**4'**) δ 126.8 (**5'**), δ 119.1 (**5**), δ 109.8 (**4**) δ 106.5 (**3**), δ 31.2 (**6'**)

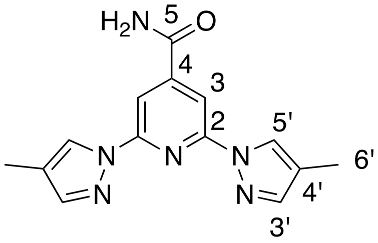

Yield: 0.12 g

MP: 219-234 °C

FTIR: {CO} 1692.58 cm^{-1} {NH} 3353.27 cm^{-1}, 3309.35 cm^{-1}

Mass Spec: $[M+H]^+$ 283.1201 m/z Calc. 283.1307 m/z

NMR: ^{1}H-NMR: (400 MHz, $(CD_3)_2SO$) δ 8.73 (s, 2H, **5’**), δ 8.11 (s, 2H, **3’**), δ 7.73 (s, 2H, **3**), δ 2.16 (s, 6H, **6’**)

^{13}C-NMR: (400 MHz, $(CD_3)_2SO$) δ 167.3 (**5**), δ 150.8 (**2**), δ 146.8 (**3’**), δ 144.0 (**4**), δ 126.1 (**4’**), δ 119.3 (**5’**), δ 106.87 (**3**), δ 9.04 (**6’**)

Synthesis of 2,6-bis(4-chloro-1H-pyrazol-1-yl)isonicotinonitrile L3

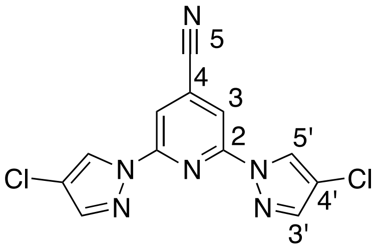

Diethylene glycol dimethyl ether (60 ml) was added to a round bottom flask with a stir bar. Sodium hydride 60% dispersion (w/w) in mineral oil (0.58 g, 14.5 mmol) was added giving a cloudy suspension. 4-Chloropyrazole (1.482 g, 14.5 mmol) was added slowly, giving off bubbles of H_2 gas. The solution was stirred for 30 minutes under nitrogen. A yellow solution was obtained, 2,6-dichloroisonicotinonitrile (1.00 g, 5.78 mmol) was added to the solution. The mixture was refluxed at 130°C for 24 hrs. Giving a white suspension. The reaction mixture was allowed to cool to room temperature and quenched with excess water. The white precipitate was filtered off and washed with water and hexane. The white powder was dried *in vacuo.*

Yield: 0.79 g, 45%

MP: 171-174 °C

FTIR: {CN} 2219.58 cm^{-1}

Mass Spec: $[M+H]^+$ 305.1595 m/z Calc. 305.0109 m/z

NMR: ^{1}H-NMR (400 MHz, $CDCl_3$) δ 8.50 (s, 2H, **3'**), δ 8.07 (s, 2H, **5'**), δ 7.74 (s, 2H, **3**)

^{13}C-NMR (400 MHz $CDCl_3$) δ 151.4 (**2**), δ 139.3 (**3'**), δ 130.6 (**4'**), δ 129.5 (**5'**), 119.6 (**5**), δ 111.2 (**4**), δ 107.2 (**3**)

Synthesis of 2,6-bis(4-bromo-1H-pyrazol-1-yl)isonicotinonitrile L4

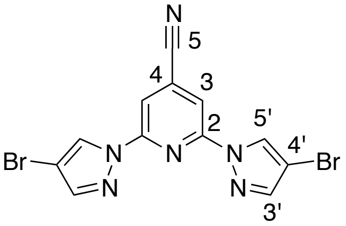

Diethylene glycol dimethyl ether (60 ml) was added to a round bottom flask with a stir bar. Sodium hydride 60% dispersion (w/w) in mineral oil (0.58 g, 14.5 mmol) was added giving a cloudy suspension. 4-Bromopyrazole (2.14 g, 14.5 mmol) was added slowly, giving off bubbles of H_2 gas. The solution was stirred for 30 minutes under nitrogen. A yellow solution was obtained, 2,6-dichloroisonicotinonitrile (1.00 g, 5.78 mmol) was added to the solution. The mixture was refluxed at 130°C for 24 hrs. Giving a white suspension. The reaction mixture was allowed to cool to room temperature and quenched with excess water. The white precipitate was filtered off and washed with water and hexane. The white powder was dried *in vacuo.*

Yield: 1.33 g, 58 %

MP: 173-176 °C

FTIR: {CN} 2218.68 cm^{-1}

Mass Spec: $[M+H]^+$ 392.9065 m/z Calc. 392.9099 m/z

NMR: ^{1}H-NMR (400 MHz, $CDCl_3$) δ 8.50 (s, 2H, **3'**), δ 8.07 (s, 2H, **5'**), δ 7.74 (s, 2H, **3**)

^{13}C-NMR (400 MHz $CDCl_3$) δ 151.4 (**2**), δ 139.3 (**3'**), δ 130.6 (**4'**), δ 129.5 (**5'**), 119.6 (**5**), δ 111.2 (**4**), δ 107.2 (**3**)

Synthesis of 2,6-bis(4-methyl-1H-pyrazol-1-yl)-4-methylpyridine L5

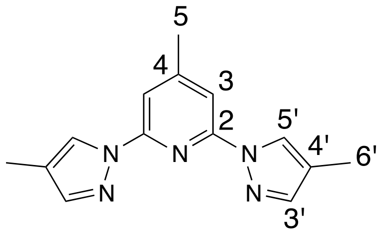

Diethylene glycol dimethyl ether (40 ml) was added to a round bottom flask. Sodium hydride 60% dispersion (w/w) in mineral oil (0.308 g, 7.7 mmol) was added giving a cloudy suspension. 4-Methylpyrazole (0.66 ml, 7.7 mmol) was added slowly, giving off bubbles of H_2 gas. The solution was stirred for 30 minutes under nitrogen. A yellow solution was obtained, 2,6-dichloropicoline (0.5 g, 3.08 mmol) was added to the solution. The solution was refluxed at 130°C for 3 days giving a white precipitate. The reaction was quenched with excess water. The precipitate was filtered and washed with water. The white powder was dried *in vacuo*.

Yield: 0.63 g, 81%

MP: 141-143 °C

Mass Spec: $[M+Na]^+$ 276.1218 m/z Calc. 276.1225 m/z

NMR: ^{1}H-NMR (400 MHz, $CDCl_3$) δ 8.33 (s, 2H, **5’**), δ 7.62 (s, 2H, **3**), δ 7.56 (s, 2H, **3’**), δ 2.27 (s, 3H, **5**), δ 2.19 (s, 6H, **6’)**

^{13}C-NMR (400 MHz, $CDCl_3$) δ 153.0 (**3**), δ 150.0 (**2**), δ 143.0 (**3’**), δ 125.5 (**4’**), δ 118.3 (**5’**), δ 109.2 (**3**), δ 21.53 (**5**), δ 9.05 (**6’**)

Synthesis of 2,6-bis(4-chloro-1H-pyrazol-yl)-4-methylpyridine L6

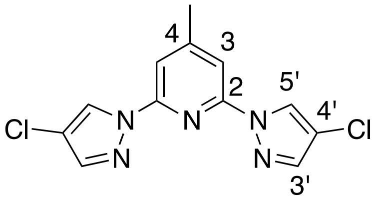

Diethylene glycol dimethyl ether (40 ml) was added to a round bottom flask. Sodium hydride 60% dispersion (w/w) in mineral oil (0.308 g, 7.7 mmol) was added giving a cloudy suspension. 4-Chloropyrazole (0.79 g, 7.7 mmol) was added slowly, giving off bubbles of H_2 gas. The solution was stirred for 30 minutes under nitrogen. A yellow solution was obtained, 2,6-dichloropicoline (0.5 g, 3.08 mmol) was added to the solution. The solution was refluxed at 130°C for 3 days giving a white precipitate. The reaction was quenched with excess water. The precipitate was filtered and washed with water and hexane. The white powder was dried *in vacuo*.

Yield: 0.41 g, 45.4 %

MP: 172-175 °C

Mass Spec: $[M+Na]^+$ 316.0124 m/z Calc. 316.0133 m/z

NMR: ^{1}H-NMR (400 MHz $CDCl_3$) δ 8.52 (s, 2H, **5'**), δ 7.69 (s, 2H, **3'**), δ 7.67 (s, 2H, **3**), δ 2.51 (s, 3H, **5**)

^{13}C-NMR (400 MHz $CDCl_3$) δ 154.2 (**4**), δ 149.7 (**2**), δ 141.0 (**3'**), δ 125.3 (**5'**), δ 113.5 (**4'**), δ 110.40 (**3**), δ 21.97 (**5**)

Synthesis of 2,6-bis(4-bromo-1H-pyrazol-yl)-4-methylpyrdine L7

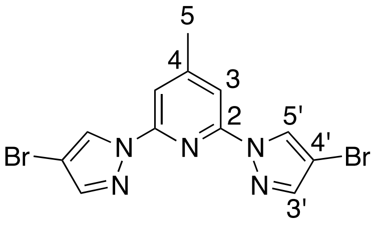

Diethylene glycol dimethyl ether (40 ml) was added to a round bottom flask. Sodium hydride 60% dispersion (w/w) in mineral oil (0.308 g, 7.7 mmol) was added giving a cloudy suspension. 4-Bromopyrazole (1.13 g, 7.7 mmol) was added slowly, giving off bubbles of H_2 gas. The solution was stirred for 30 minutes under nitrogen. A yellow solution was obtained, 2,6-dichloropicoline (0.5 g, 3.08 mmol) was added to the solution. The solution was refluxed at 130°C for 3 days giving a white precipitate. The reaction was quenched with excess water. The precipitate was filtered and washed with water and hexane. The white powder was dried *in vacuo*.

Yield: 0.74 g, 63%

MP: 178-180 °C

Mass Spec: [M+H_2O] 400.423 m/z Calc. 400.9310 m/z

NMR ^{1}H-NMR (400 MHz $CDCl_3$) δ 8.56 (s, 2H, **5’**) δ 7.70 (d, 4H, **3 3’**) δ 2.51 (s, 3H, **5**)

^{13}C-NMR (400 MHz $CDCl_3$) δ 153.9 (**4**), δ 149.2 (**2**), δ 142.7 (**3**), δ 127.2 (**5’**), δ 110.1 (**3**), δ 96.6 (**4’**), δ 21.6 (**5**)

3.3 Reduction of L^1

Synthesis of *tert*-butyl ((2,6-di(1*H*-pyrazol-1-yl)pyridine-4-yl)methyl)carbamate

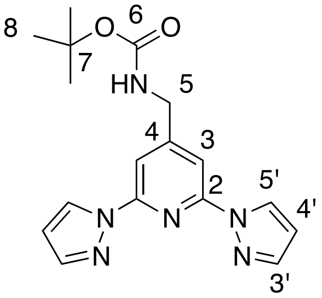

2,6-di(1*H*-pyrazol-1-yl)isonicotinonitrile (**L1**) (0.5 g, 2.12 mmol) was dissolved in dry methanol (150 ml). The solution was kept at 0° C. Di-tert-butyl dicarbonate (1.61 g, 7.41 mmol) was added to the clear solution. The solution was stirred for 1 hour. $NiCl_2 \cdot 6H_2O$ (0.055 g, 0.212 mmol) was added giving a green solution. $NaBH_4$ (0.585 g, 15.47 mmol) was added slowly instantly giving a black solution with the evolution of H_2 gas. The reaction was left to stir at room temperature for 24 hours. A green solution was observed indicating that all the $NaBH_4$ had been used up. Diethylenetriamine (1 ml, 10.1 mmol) was added to the solution. The solution was stirred for 1 hour. The solvent was removed *in vacuo* giving a pink wax. The wax dissolved in ethyl acetate (200 ml) and washed with two 50 ml aliquots of saturated $NaHCO_3$ solution. The organic layer was collected and dried with anhydrous $MgSO_4$. The solvent was then removed *in vac*uo giving a white powder.

Yield: 0.72 g, 68%

MP: 141-147 °C

FTIR: {CO} 1682.38 cm^{-1} {NH} 3362.91 cm^{-1}

Mass Spec: $[M+H]^+$ 341.1006 m/z Calc. 341.1726 m/z

NMR: ^{1}H-NMR (400 MHz $CDCl_3$) δ 8.48 (d, 2H, J= 2.44 Hz, **5’**), δ 7.71 (s, 4H, **3**, **3’**), δ 6.44 (dd, 2H, J= 4.2 Hz, J= 0.87 Hz, **4’**), δ 4.41 (s, 2H, **5**), δ 1.45 (s, 9H, **8**)

^{13}C-NMR (400 MHz $CDCl_3$) δ 164.96 (**6**), δ 149.9 (**2**), δ 147.7 (**3’**), δ 142.7 (**4**), δ 128.1 (**5’**), δ 108.5 (**4’**), δ 106.8 (**3**), δ 79.9 (**7**), δ 53.0 (**5**), δ 28.0 (**8**)

Synthesis of (2,6-di(1*H*-pyrazol-1-yl)pyridin-4-yl)methanamine Hydrochloride

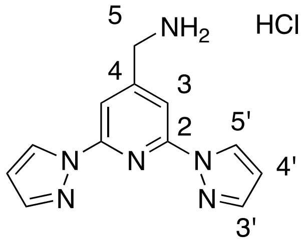

Acetyl chloride (10ml, 140 mmol) was added to a stirring solution of dry methanol (70 ml) slowly at 0°C in a round bottom flask. The reaction was exothermic. The solution was stirred for 1 hour and the pH was monitored using Litmus paper. When the pH was 1 tert-butyl ((2,6-di(1*H*-pyrazol-1-yl)pyridine-4-yl)methyl)carbamate (0.6 g, 1.77 mmol) was added and slowly dissolved to give a green solution. The flask was stoppered and the reaction was allowed to stir for 24 hours at room temperate. A white precipitate was then observed. The precipitate was then filtered and dried *in vacuo*.

Yield: 0.45 g, 92%

Mass Spec: $[M+H]^+$ 242.2831 m/z Calc. 242.2849 m/z

NMR: ^{1}H-NMR (400 MHz $(CD_3)_2SO$) δ 10.11 (1H, N**H**) , δ 8.98 (d, 2H, J= 1.4 Hz, **5’**), δ 8.66 (1H, N**H**), δ 8.39 (1H, N**H**), δ 7.98 (s, 2H, **3**), δ 7.90 (d, 2H, J= 0.60 Hz, **3’**), δ 6.66 (dd, 2H, J= 1.28 Hz, **4’**), δ 4.27 (q, 2H, J= 7.04 Hz , **5**)

^{13}C-NMR (400 MHz $(CD_3)_2SO$) δ 150.3 (**2**), δ 143.40(**4**), δ 143.4 (**3’**) δ 128.9 (**5’**), δ 109.2 (**4’**), δ 109.2 (**3**) 41.8 (**5**)

Synthesis of (2,6-di(1*H*-pyrazol-1-yl)pyridin-4-yl)methanamine L8

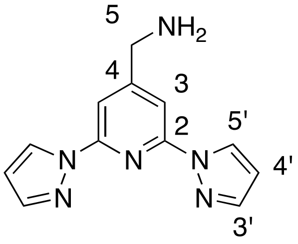

(2,6-di(1*H*-pyrazol-1-yl)pyridin-4-yl)methanamine hydrochloride (0.4 g, 1.45 mmol) was dissolved in water (100 ml). Sodium bicarbonate was added to the stirring solution until the evolution of CO_2 gas had stopped. Chloroform (40 ml) was added to the solution. The mixture was stirred for 2 hours. The organic layer was collected and washed with brine (30 ml) and dried with anhydrous magnesium sulfate. The solvent was removed *in vacuo* to yield a white powder.

Yield: 0.27 g, 78%

MP: 169-171 °C

FTIR: {NH} 3346.83 cm^{-1}, 3347.59 cm^{-1}

Mass Spec: $[M+H]^+$ 240.9899 Calc. 241.1202

NMR: ^{1}H-NMR (400 MHz $CDCl_3$) δ 8.59 (d, J= 1.36 Hz , 2H, **5'**), δ 7.86 (s, 2H, **3**), δ 7.77 (d, J= 0.64, 2H, **3**'), δ 6.51 (dd, J= 2.18 Hz , 2H, **4'**), δ 4.05 (s, 2H, **5**)

^{13}C-NMR (400 MHz $CDCl_3$) δ 150.8 (**2**), δ 147.2 (**3'**), δ 142.9 (**4**), δ 127.7 (**5'**), δ 108.5 (**4'**), δ 107.7 (**3**), δ 53.0 (**5**)

3.4 Complexations

Synthesis of $[Fe(L^1)_2][BF_4]_2$ (1a)

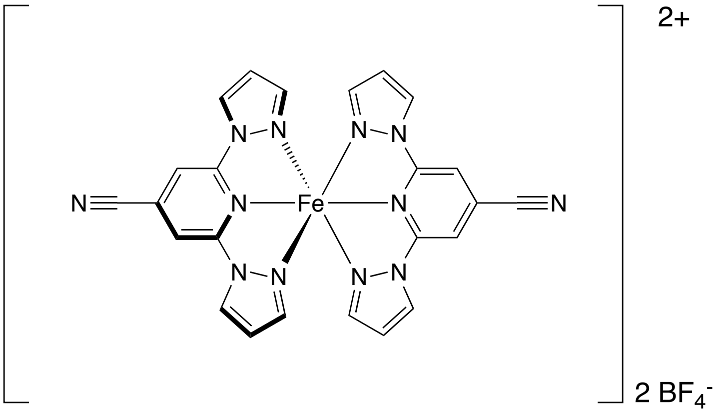

2,6-di(1*H*-pyrazol-1-yl)isonicotinonitrile (**L1**) (0.1 g, 0.42 mmol) was dissolved in nitromethane (20 ml) giving a clear solution. Iron(II) tetrafluoroborate hexahydrate (0.071 g, 0.21 mmol) was added to the solution, producing a dark red colour. The solution was stirred for 30 minutes and concentrated to approximately 5 ml *in vacuo*. Bright orange thin plate crystals were then obtained by slow diffusion with diethyl ether.

Yield: 0.073 g, 50%

NMR: ^{1}H-NMR: (300 MHz, CD_3CN) δ 44.08 (s, 4H, **3’**), δ 41.56 (s, 4H, **4’**), δ 27.78 (s, 4H, **5’**),
δ 24.18 (s, 4H, **3**)

CHN Analysis: $C_{24}H_{16}N_{12}FeB_2F_8$	Calculated:	C 41.06	H 2.29	N 23.95
	Found:	C 40.94	H 2.17	N 23.75

Synthesis of [Fe(L^1)$_2$][ClO$_4$]$_2$ (1b)

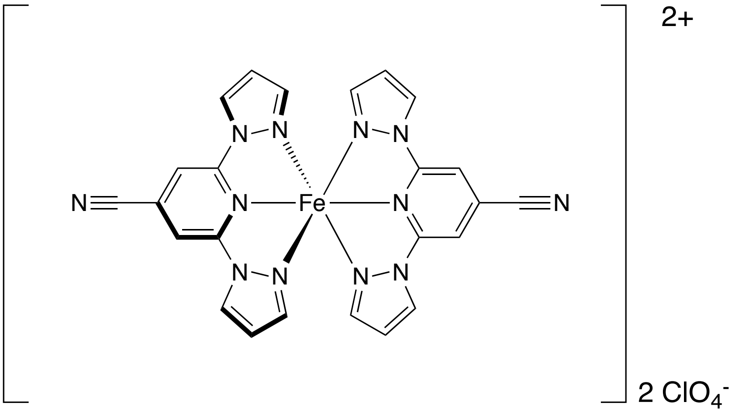

2,6-di(1*H*-pyrazol-1-yl)isonicotinonitrile (**L1**) (0.1 g, 0.42 mmol) was dissolved in nitromethane (20 ml) giving a clear solution. Iron(II) perchlorate hexahydrate (0.076 g, 0.21 mmol) was added to the solution producing a dark red colour. The solution was stirred for 30 minutes and concentrated to approximately 5 ml *in vacuo*. Dark red single crystals were then obtained by slow diffusion with diethyl ether.

Yield:

CHN Analysis: $C_{24}H_{16}N_{12}FeCl_2O_8$	Calculated:	C 39.64	H 2.22	N 23.11
	Found:	C 39.41	H 2.25	N 23.07

Synthesis of [Fe(L^1)$_2$][OTf]$_2$ (1c)

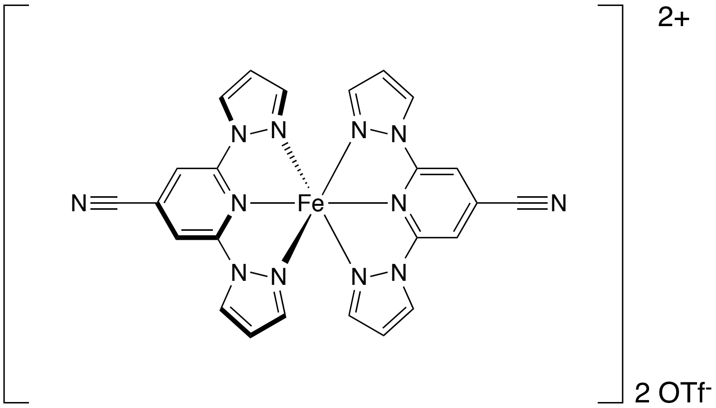

2,6-di(1*H*-pyrazol-1-yl)isonicotinonitrile (**L1**) (0.1 g, 0.42 mmol) was dissolved in nitromethane (20 ml) giving a clear solution. Iron(II) trifluoromethanesulfonate (0.075 g, 0.21 mmol) was added to the solution producing a dark red colour. The solution was stirred for 30 minutes and concentrated to approximately 5 ml *in vacuo*. Dark red single crystals were obtained by slow diffusion of diethyl ether.

Yield:

CHN Analysis: $C_{26}H_{26}N_{12}FeF_6O_6S_2$	Calculated:	C 37.79	H 1.95	N 20.34
	Found:	C 37.68	H 1.86	N 20.26

Synthesis of $[Fe(L^2)_2][BF_4]_2$ (2)

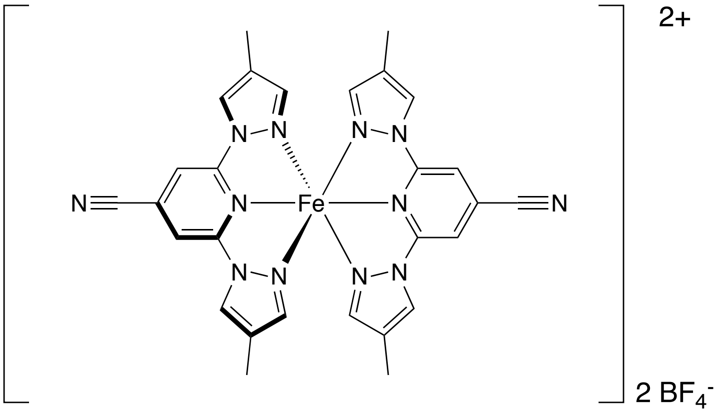

2,6-di(4-methyl-1*H*-pyrazol-1-yl)isonicotinonitrile (**L2**) (0.11 g, 0.42 mmol) was dissolved in nitromethane (20 ml) giving a clear solution. Iron(II) tetrafluoroborate hexahydrate (0.071 g, 0.21 mmol) was added to the solution producing a dark red colour. The solution was stirred for 20 minutes and concentrated to approximately 5 ml *in vacuo*. Dark red needle crystals were obtained by slow diffusion by diethyl ether.

Yield: 0.053 g, 33%

NMR: ^{1}H-NMR: (300 MHz, CD$_3$CN) δ 41.87 (s, 4H, **3**), δ 28.29 (s, 4H, **3’**) δ 26.74 (s, 4H, **5’**) δ 2.27 (s, 12H, **6’**)

CHN Analysis: $C_{28}H_{24}N_{12}FeB_2F_8$	Calculated:	C 44.37	H 3.19	N 22.17
	Found:	C 42.48	H 3.34	N 22.31

Synthesis of $[Fe(L^3)_2][BF_4]_2 \cdot 1\ MeNO_2$ (3)

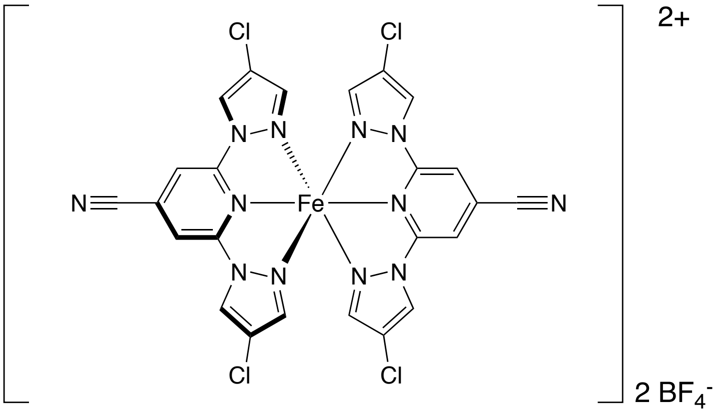

2,6-di(4-chloro-1*H*-pyrazol-1-yl)isonicotinonitrile (**L3**) (0.256 g, 0.42 mmol) was dissolved in nitromethane (20 ml) giving a clear solution. Iron(II) tetrafluoroborate hexahydrate (0.071 g, 0.21 mmol) was added to the solution producing a dark red colour. The solution was stirred for 30 minutes and concentrated to approximately 5 ml *in vacuo*. Dark red single crystals were obtained by slow diffusion with diethyl ether.

Yield: 0.037 g, 21%

Mass Spec: $[Fe(L)_1(CH_3O^-)]^+$ 393.1300 m/z Calc. 393.0090 m/z

NMR: ^{1}H-NMR: (300 MHz, CD_3COCD_3): δ 50.02 (s, 4H, **3'**) δ 46.79 (s, 4H, **5'**) δ 33.27 (s, 4H, **3**)

CHN Analysis: $C_{24}H_{12}N_{12}FeCl_4B_2F_8$	Calculated:	C 33.61	H 1.65	N 19.60
	Found:	C 33.31	H 1.74	N 20.29

Synthesis of $[Fe(L^4)_2][BF_4]_2$ (4)

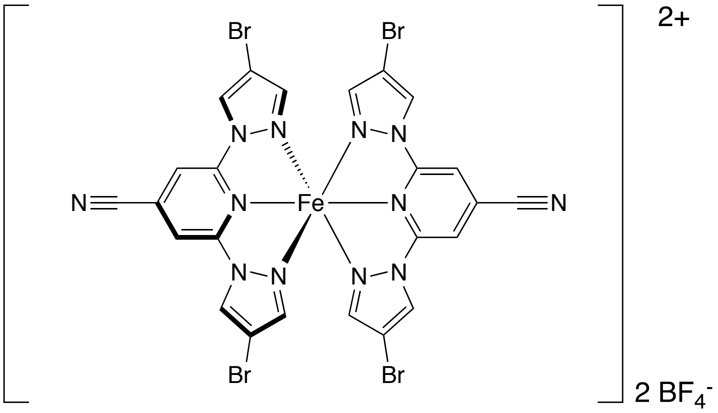

2,6-di(4-bromo-1*H*-pyrazol-1-yl)isonicotinonitrile (**L4**) (0.33 g, 0.42 mmol) was dissolved in nitromethane (20 ml) giving a clear solution. Iron(II) tetrafluoroborate hexahydrate (0.071 g, 0.21 mmol) was added to the solution producing a dark red colour. The solution was stirred for 30 minutes and concentrated to approximately 5 ml *in vacuo*. Dark red single crystals were obtained by slow diffusion with diethyl ether.

Yield: 0.0555 g, 26%

NMR: ^{1}H-NMR: (300 MHz, CD_3COCD_3): δ 52.22 (s, 4H, **3'**) δ 48.38 (s, 4H, **5'**), δ 35.96 (s, 4H, **3**)

CHN Analysis: $C_{24}H_{12}N_{12}FeBr_4B_2F_8$	Calculated:	C 27.36	H 1.53	N 15.95
	Found:	C 26.87	H 1.84	N 15.19

Synthesis of [Fe(L^5)$_2$][BF$_4$]$_2$ (5a)

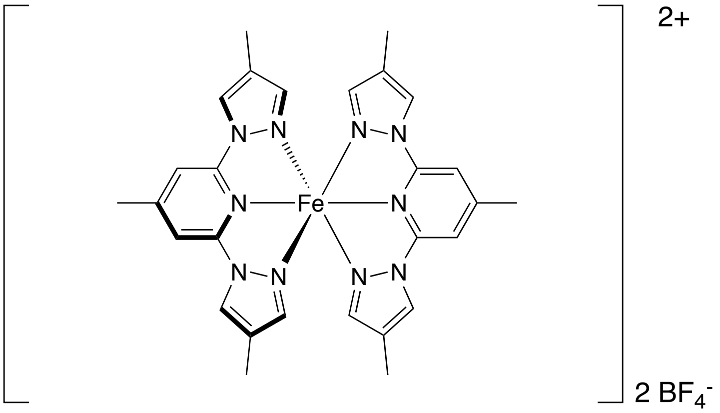

2,6-bis(4-methyl-1H-pyrazol-1-yl)-4-methylpyridine (**L5**) (0.212 g, 0.42 mmol) was dissolved in nitromethane (20 ml) giving a clear solution. Iron(II) tetrafluoroborate hexahydrate (0.071 g, 0.21 mmol) was added to the solution producing a bright orange colour. The solution was stirred for 30 minutes and concentrated to approximately 5 ml *in vacuo*. Brown crystals were obtained by slow diffusion with diethyl ether.

Yield: 0.105 g, 67%

NMR: ^{1}H-NMR: (300 MHz, CD_3COCD_3): δ 59.03 (s, 4H, **3'**), δ 40.49 (s, 8H, **3, 5'**)

CHN: Analysis: $C_{28}H_{30}N_{10}FeB_2F_8$	Calculated:	C 45.69	H 4.11	N 19.03
	Found:	C 44.13	H 3.97	N 18.42

Synthesis of [Fe(L^5)$_2$][ClO$_4$]$_2$ (5b)

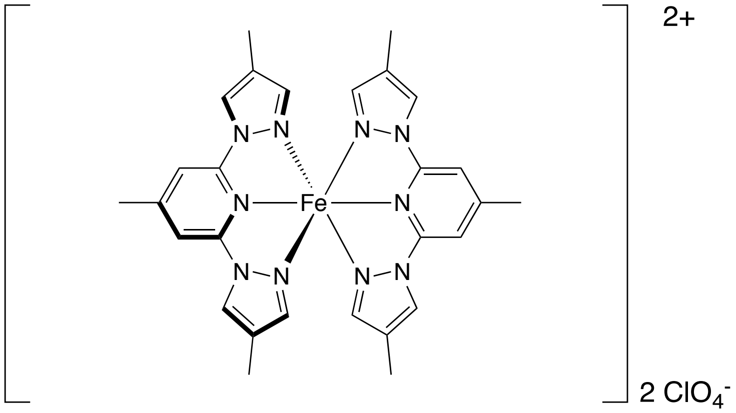

2,6-bis(4-methyl-1H-pyrazol-1-yl)-4-methylpyridine (**L5**) (0.212 g, 0.42 mmol) was dissolved in nitromethane (20 ml) giving a clear solution. Iron(II) perchlorate (0.076 g, 0.21 mmol) was added to the solution producing a bright orange colour. The solution was stirred for 30 minutes and concentrated to approximately 5 ml *in vacuo*. Brown crystals were obtained by slow diffusion with diethyl ether.

Yield: 0.075 g, 47%

CHN: Analysis: $C_{28}H_{30}N_{10}FeCl_2O_8$	Calculated:	C 44.17	H 3.97	N 18.40
	Found:	C 41.51	H 3.85	N 17.17

Synthesis of [Fe(L^5)$_2$][OTf]$_2$ (5c)

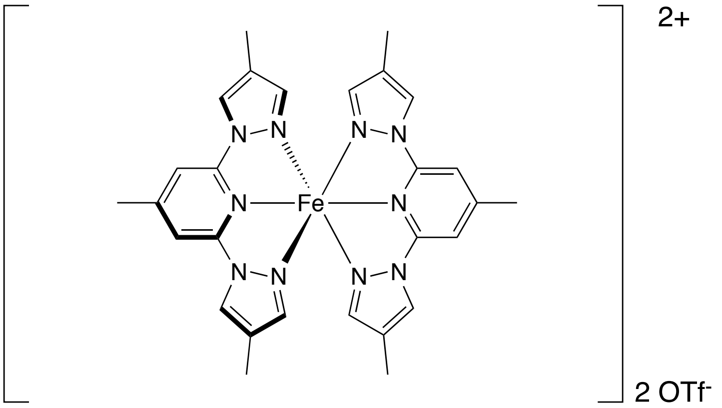

2,6-bis(4-methyl-1H-pyrazol-1-yl)-4-methylpyridine (**L5**) (0.212 g, 0.42 mmol) was dissolved in nitromethane (20 ml) giving a clear solution. Iron(II) trifluoromethanesulfonate (0.075 g, 0.21 mmol) was added to the solution producing a bright orange colour. The solution was stirred for 30 minutes and concentrated to approximately 5 ml *in vacuo*. Brown crystals were obtained by slow diffusion with diethyl ether.

Yield: 0.110 g, 61%

CHN: Analysis: $C_{30}H_{30}N_{10}FeF_6O_6S_2$	Calculated:	C 41.87	H 3.51	N 16.28
	Found:	C 41.72	H 3.49	N 16.19

Synthesis of [Fe(L^6)$_2$][BF$_4$]$_2$ (6)

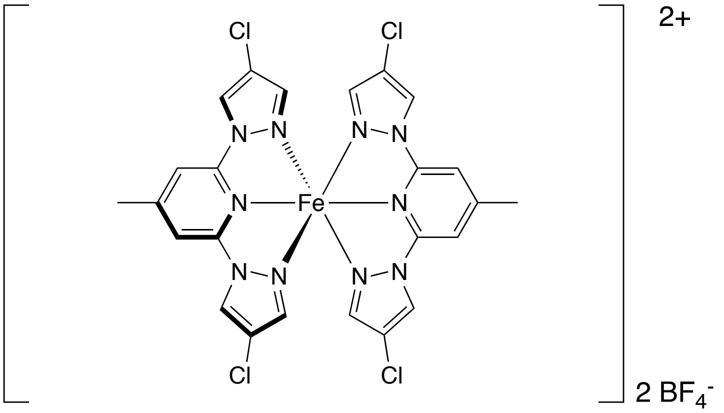

2,6-bis(4-chloropyrazol-1-yl)-4-methypyridine (**L6**) (0.246 g, 0.42 mmol) was dissolved in nitromethane (20 ml) giving a clear solution. Iron(II) tetrafluoroborate hexahydrate (0.071 g, 0.21 mmol) was added to the solution producing a bright orange colour. The solution was stirred for 30 minutes and concentrated to approximately 5 ml *in* vacuo. Dark red crystals were obtained by slow diffusion with diethyl ether.

Yield: 0.053 g, 31%

NMR: ^{1}H-NMR: (300 MHz, CD_3COCD_3): δ 65.00 (s, 4H, **3'**), δ 52.71 (s, 8H, **5', 3**)

CHN: Analysis: $C_{26}H_{24}N_{10}FeCl_4B_2F_8$	Calculated:	C 35.25	H 2.22	N 17.13
	Found:	C 35.25	H 2.28	N 17.02

Synthesis of $[Fe(L^7)_2][BF_4]_2$ (7)

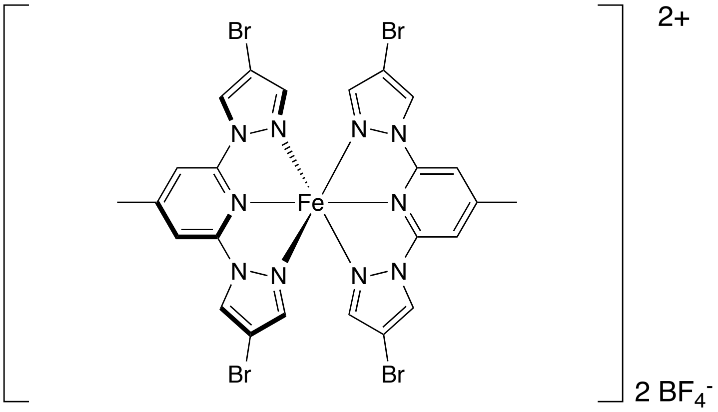

2,6-bis(4-bromopyrazol-1-yl)-4-methylpyridine (**L7**) (0.318 g, 0.42 mmol) was dissolved in nitromethane (20 ml) giving a clear solution. Iron(II) tetrafluoroborate hexahydrate (0.071 g, 0.21 mmol) was added to the solution producing a bright orange colour. The solution was stirred for 30 minutes and concentrated to approximately 5 ml *in vacuo*. Dark red crystals were obtained by slow diffusion with diethyl ether.

Yield: 0.0565 g, 27%

NMR: ^{1}H-NMR: (300 MHz, CD_3COCD_3): δ 64.29 (2, 4H, **3'**), δ 51.23 (s, 8H, **5', 3**)

CHN: Analysis: $C_{26}H_{24}N_{10}FeBr_4B_2F_8$	Calculated:	C 28.95	H 1.82	N 14.07
	Found:	C 28.83	H 1.95	N 13.99

Synthesis of $[Fe(L^8)_2][ClO_4]_2$ (8)

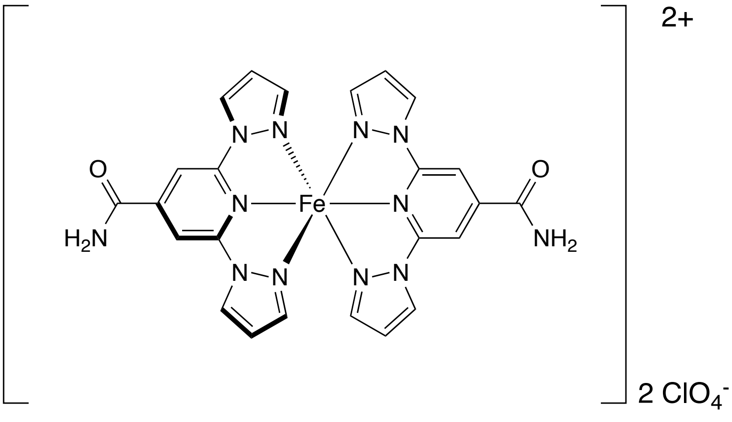

(2,6-di(1*H*-pyrazol-1-yl)pyridin-4-yl)methanamine (**L8**) (0.101 g, 0.42 mmol) was dissolved in nitromethane (20 ml) giving a clear solution. Iron(II) perchlorate hexahydrate (0.076 g, 0.21 mmol) was added to the solution producing a dark red colour. The solution was stirred for 30 minutes and concentrated to approximately 5 ml *in vacuo*. Dark brown crystals were obtain by slow diffusion with diethyl ether.

Yield: 0.075 g, 47%

NMR: ^{1}H-NMR: (300 MHz, CD_3COCD_3): δ 49.58 (s, 4H, **3'**) δ 46.08 (s, 4H, **4'**) δ 31.31 (s, 4H, **5'**) δ 28.16 (s, 4H, **3**)

CHN Analysis: $C_{24}H_{20}N_{12}FeCl_2O_{10}$	Calculated:	C 37.77	H 2.64	N 22.02
	Found:	C 37.26	H 2.44	N 21.71

Synthesis of $[Ag_2(L^1)_2][BF_4]_2$. 0.5 $MeNO_2$

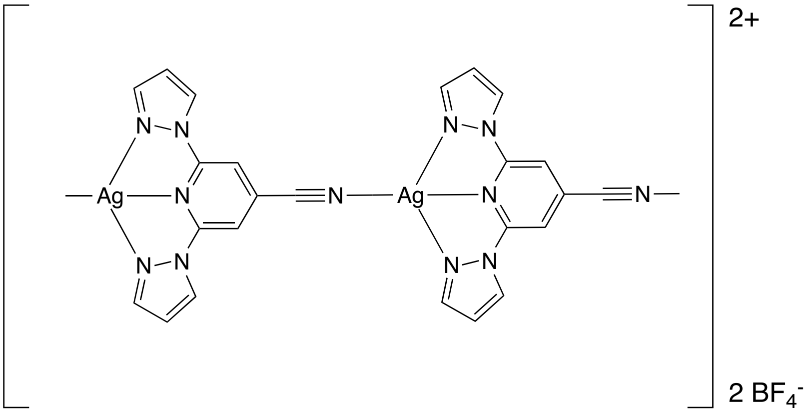

a) 2,6-di(1*H*-pyrazol-1-yl)isonicotinonitrile (**L1**) (0.05 g, 0.21 mmol) was added to a stirring solution of nitromethane (10 ml). The solution was heated to 40°C, silver(I) tetrafluoroborate (0.04 g, 0.21 mmol) was added to the solution. The solution was stirred for 2 hours. Colorless crystals were obtained by slow diffusion with diethyl ether.

b) **1a** (0.05 g, 0.07 mmol) was dissolved in nitromethane (5 ml). Silver(I) tetrafluoroborate (0.027 g, 0.14 mmol) was added to the stirring solution. The solution was stirred for 1 hour, colorless crystals were obtained by slow diffusion with diethyl ether.

Yield: a) 0.059 g ,64% b) 0.02 g, 17%

CHN: Analysis: $C_{25}H_{19}N_{13}Ag_2O_2B_2F_8$	Calculated:	C 32.54	H 2.08	N 19.73
	Found:	C 32.11	H 1.97	N 19.45

Synthesis of $[Mn(L^1)(hfac)_2]$.1 $MeNO_2$

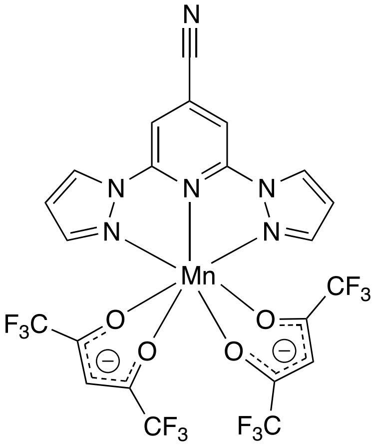

2,6-di(1*H*-pyrazol-1-yl)isonicotinonitrile (**L1**) (0.1 g, 0.21 mmol) was dissolved in nitromethane (20 ml). Manganese(II) hexa-fluoroacetylacetonato trihydrate (0.055 g, 0.105 mmol) was added to the solution giving a pale yellow color. The solution was stirred for 2 hours and concentrated to approximately 10 ml in vacuo. Pale yellow crystals were obtained by slow diffusion with diethyl ether.

Yield: 0.09 g, 61%

CHN: Analysis: $C_{23}H_{17}N_7MnO_6F_{12}$	Calculated:	C 35.86	H 2.22	N 12.73
	Found:	C 34.48	H 2.73	N 13.48

References:

(1) Van Vleck, J. H. *Phys. Rev.* **1932**, *41* (2), 208–215.

(2) Tsuchida, R. *Bull. Chem. Soc. Jpn.* **1938**, *13* (5), 388–400.

(3) Tsuchida, R. *Bull. Chem. Soc. Jpn.* **1938**, *13* (6), 436–450.

(4) Griffith, J. S.; Orgel, L. E. *Q. Rev. Chem. Soc.* **1957**, *11* (4), 381–393.

(5) Gütlich, P. *Eur. J. Inorg. Chem.* **2013**, No. 5–6, 581–591.

(6) De Graaf, C.; Sousa, C. *Chem. - A Eur. J.* **2010**, *16* (15), 4550–4556.

(7) Gütlich, P.; Ksenofontov, V.; Gaspar, A. B. In *Coordination Chemistry Reviews*; (5-6), **2005** 770-780.

(8) Cambi, L.; Szegö, L. Berichte der Dtsch. Chem. Gesellschaft (A B Ser. **1931**, 64 (10), 2591–2598.

(9) Miyamachi, T.; Gruber, M.; Davesne, V.; Bowen, M.; Boukari, S.; Joly, L.; Scheurer, F.; Rogez, G.; Yamada, T. K.; Ohresser, P.; Beaurepaire, E.; Wulfhekel, W. Nat. Commun. **2012**, 936–938.

(10) Real, J. A.; Gaspar, A. B.; Muñoz, M. C. Dalton Trans. **2005**, No. 12, 2062–2079.

(11) Gutlich, P.; Goodwin, H. Spin Crossover Transit. Met. Compd. I **2004**, 233, 1–47.

(12) Shatruk, M.; Avendano, C.; Dunbar, K. R. Prog. Inorg. Chem. **2009**, 56, 155–334.

(13) Gütlich, P.; Hauser, A.; Spiering, H. Angew Chemie- Int. Ed. **1994**, pp 2024–2054.

(14) Letard, J. F.; Guionneau, P.; Codjovi, E.; Lavastre, O.; Bravic, G.; Chasseau, D.; Kahn, O. J. Am. Chem. Soc. **1997**, 119 (44), 10861–10862.

(15) Berezovskii, G. A.; Lavrenova, L. G. J. Therm. Anal. Calorim. **2011**, 103 (3), 1063–1072.

(16) König, E. *Complex Chemistry* **1991**, 51-152.

(17) Chakraborty, P.; Enachescu, C.; Hauser, A. *Eur. J. Inorg. Chem.* **2013**, (5-6), 770-780.

(18) Hauser, A.; Adler, P.; Deisenroth, S.; Gütlich, P.; Hennen, C.; Spiering, H.; Vef, A. *Hyperfine Interact.* **1994**, 33, 2024-2054.

(19) Buchen, T.; Guetlich, P.; Goodwin, H. A. *Inorg. Chem.* **1994**, *33* (20), 4573–4576.

(20) Konig, E.; Madeja, K. *Inorg. Chem.* **1967**, *6* (1), 48–55.

(21) Elhaik, J.; Evans, D. J.; Kilner, C. A.; Halcrow, M. A. *Dalt. Trans.* **2005**, No. 9, 1693–1700.

(22) Tuchagues, J.-P.; Bousseksou, A.; Molnar, G.; McGarvey, J. J.; Varret, F. *Top. Curr. Chem.* **2004**, 84-103.

(23) Halcrow, M. A. *Polyhedron* **2007**, 26 (14), 3525-3576.

(24) Holland, J. M.; McAllister, J. A.; Kilner, C. A.; Thornton-Pett, M.; Bridgeman, A. J.; Halcrow, M.

A. *J. Chem. Soc. Dalt. Trans.* **2002**, 4, 548-554.

(25) Halcrow, M. A. *Chemical Society Reviews*. **2011**, 40, 4119-4142.

(26) Elhaïk, J.; Kilner, C. A.; Halcrow, M. A. *Dalt. Trans.* **2006**, (6), 823-830.

(27) Nihei, M.; Tahira, H.; Takahashi, N.; Otake, Y.; Yamamura, Y.; Saito, K.; Oshio, H. *J. Am. Chem. Soc.* **2010**, 132 (10), 3553-3560.

(28) Weber, B.; Tandon, R.; Himsl, D. *Zeitschrift fur Anorg. und Allg. Chemie* **2007**, *633* (8), 1159–1162.

(29) Bronisz, R. *Inorg. Chem.* **2005**, *44* (13), 4463–4465.

(30) Krober, J.; Codjovi, E.; Kahn, O.; Grolibre, F.; Jay$, C. *J. Am. Chem. SOC* **1993**, *115*, 9810–9811.

(31) Braga, D.; Grepioni, F. *Making Crystals by Design: Methods, Techniques and Applications*; **2007**, 1-346.

(32) Han, W. K.; Qin, L. F.; Pang, C. Y.; Cheng, C. K.; Zhu, W.; Li, Z. H.; Li, Z.; Ren, X.; Gu, Z. G. *Dalt. Trans.* **2017**, 46 (25), 8004-8008.

(33) Tao, J.; Wei, R. J.; Huang, R. Bin; Zheng, L. S. *Chemical Society Reviews*. **2012**, 41, 703-737.

(34) Boukheddaden, K.; Traiche, R.; Oubouchou, H.; Linares, J. *Magnetochemistry* **2016**, 2 (1), 17.

(35) Lang, A. R. *Acta Metall.* **1956**, 4 (1), 102.

(36) Hasegawa, Y.; Kume, S.; Nishihara, H. *J. Chem. Soc. Dalt. Trans.* **2009**, 2, 280-284.

(37) Rudd, D. J.; Goldsmith, C. R.; Cole, A. P.; Stack, T. D. P.; Hodgson, K. O.; Hedman, B. *Inorg. Chem.* **2005**.

(38) Maeda, Y. *Bull. Chem. Soc. Jpn.* **1998**, 71 (12), 2837-2843.

(39) Barrett, S. A.; Kilner, C. A.; Halcrow, M. A. *Dalt. Trans.* **2011**, 40 (45), 12021-12024.

(40) Bryliakov, K. P.; Duban, E. A.; Talsi, E. P. *Eur. J. Inorg. Chem.* **2005**, 1, 72-76.

(41) Constable, E. C.; Baum, G.; Bill, E.; Dyson, R.; van Eldik, R.; Fenske, D.; Kaderli, S.; Morris, D.; Neubrand, A.; Neuburger, M.; Smith, D. R.; Wieghardt, K.; Zehnder, M.; Zuberbühler, A. D. *Chem. - A Eur. J.* **1999**, 5 (2), 498-508.

(42) Rodríguez-Jiménez, S.; Brooker, S. *Inorg. Chem.* **2017**, *56* (22), 13697–13708.

(43) Mcconnell, H. M.; Robertson, R. E. *J. Chem. Phys.* **1958**, 29 (6), 1361-1365.

(44) Schubert, E. M. *J. Chem. Educ.* **1992**, *69* (1), 62.

(45) Ni, Z.; McDaniel, A. M.; Shores, M. P. *Chem. Sci.* **2010**, 1 (5), 615-621.

(46) Ostfeld, D.; Cohen, I. A. *J. Chem. Educ.* **1972**, 49 (12), 829.

(47) Berry, J. F.; Cotton, F. A.; Lu, T.; Murillo, C. A. *Inorg. Chem.* **2003**, 42 (14), 4425-4430.

(48) Halcrow, M. A. *Coordination Chemistry Reviews*. **2005**, 249 (24), 2880-2908.

(49) Heider, S.; Petzold, H.; Speck, J. M.; Rüffer, T.; Schaarschmidt, D. *Zeitschrift fur Anorg. und Allg. Chemie* **2014**, 640 (7), 1360-1367.

(50) Santoro, A.; Kershaw Cook, L. J.; Kulmaczewski, R.; Barrett, S. A.; Cespedes, O.; Halcrow, M. A. *Inorg. Chem.* **2015**, 54 (2), 682-693.

(51) Kershaw Cook, L. J.; Kulmaczewski, R.; Mohammed, R.; Dudley, S.; Barrett, S. A.; Little, M. A.; Deeth, R. J.; Halcrow, M. A. *Angew. Chemie - Int. Ed.* **2016**, *55* (13), 4327–4331.

(52) Cook, L. J. K.; Kulmaczewski, R.; Cespedes, O.; Halcrow, M. A. *Chem. - A Eur. J.* **2016**, *22* (5), 1789–1799.

(53) Kershaw Cook, L. J.; Thorp-Greenwood, F. L.; Comyn, T. P.; Cespedes, O.; Chastanet, G.; Halcrow, M. A. *Inorg. Chem.* **2015**, *54* (13), 6319–6330.

(54) Pritchard, R.; Kilner, C. A.; Halcrow, M. A. *Chem. Commun.* **2007**, (6), 577-579.

(55) Scudder, M. L.; Goodwin, H. A.; Dance, I. G. *New J. Chem.* **1999**, 23 (7), 695-705.

(56) Holland, J. M.; McAllister, J. A.; Lu, Z.; Kilner, C. A.; Thornton-Pett, M.; Halcrow, M. A. *Chem. Commun.* **2001**, (6), 577-578.

(57) Pritchard, R.; Lazar, H.; Barrett, S. A.; Kilner, C. A.; Asthana, S.; Carbonera, C.; Létard, J. F.; Halcrow, M. A. *J. Chem. Soc. Dalt. Trans.* **2009**, (33), 6656-6666.

(58) Capel Berdiell, I.; Kulmaczewski, R.; Halcrow, M. A. *Inorg. Chem.* **2017**, 56 (17), 8817-8828.

(59) Tsuchiya, N.; Tsukamoto, A.; Ohshita, T.; Isobe, T.; Senna, M.; Yoshioka, N.; Inoue, H. *J. Solid State Chem.* **2000**, 153 (1), 82-91.

(60) Hansch, C.; Leo, A.; Taft, R. W. *Chem. Rev.* **1991**, *91* (2), 165–195.

(61) Prat, I.; Company, A.; Corona, T.; Parella, T.; Ribas, X.; Costas, M. *Inorg. Chem.* **2013**, 52 (16), 9229-9244.

(62) Nakano, K.; Suemura, N.; Yoneda, K.; Kawata, S.; Kaizaki, S. *Dalt. Trans.* **2005**, (4), 740-743.

(63) Nakano, K.; Suemura, N.; Kawata, S.; Fuyuhiro, A.; Yagi, T.; Nasu, S.; Morimoto, S.; Kaizaki, S. *J. Chem. Soc. Dalt. Trans.* **2004**, 4 (7), 982-988.

(64) Park, J. G.; Jeon, I.-R.; Harris, T. D. *Inorg. Chem.* **2015**, 54, 359-369.

(65) Lin, H.-J.; Siretanu, D.; Dickie, D. A.; Subedi, D.; Scepaniak, J. J.; Mitcov, D.; Clérac, R.; Smith, J. M. *J. Am. Chem. Soc.* **2014**, 136 (38), 13326-13332.

(66) Takahashi, K.; Hasegawa, Y.; Sakamoto, R.; Nishikawa, M.; Kume, S.; Nishibori, E.; Nishihara, H. *Inorg. Chem.* **2012**, 51 (9), 5188-5198.

(67) Jameson, D. L.; Goledsby, K. A. *J. Org. Chem.* **1990**, 55 (17), 4992-4994.

(68) Elhaïk, J.; Pask, C. M.; Kilner, C. A.; Halcrow, M. A. *Tetrahedron* **2007**, *63* (2), 291–298.

(69) Rappoport, Z. *The chemistry of the cyano group*; **1970**.

(70) George A. Jeffrey. *An Introduction to Hydrogen Bonding*; **1997**.

(71) Caddick, S.; Judd, D. B.; Lewis, A. K. D. K.; Reich, M. T.; Williams, M. R. V. *Tetrahedron* **2003**, *59* (29), 5417–5423.

(72) Arena, G.; Calogero, G.; Campagna, S.; Monsù Scolaro, L.; Ricevuto, V.; Romeo, R. *Inorg. Chem.* **1998**, 37 (11), 2763-2769.

(73) Hrobárik, P.; Reviakine, R.; Arbuznikov, A. V.; Malkina, O. L.; Malkin, V. G.; Köhler, F. H.; Kaupp, M. *J. Chem. Phys.* **2007**, 126 (2).

(74) Kilner, C. A.; Halcrow, M. A. *Acta Crystallogr. Sect. C Cryst. Struct. Commun.* **2006**, 62 (9).

(75) Smith, E.; Dent, G. *Modern Raman Spectroscopy - A Practical Approach*; **2005**.

(76) Boča, R. *Coordination Chemistry Reviews*. **2004**, 248 (9-10), 757-815.

(77) Neville, S. M.; Halder, G. J.; Chapman, K. W.; Duriska, M. B.; Southon, P. D.; Cashion, J. D.; Létard, J. F.; Moubaraki, B.; Murray, K. S.; Kepert, C. J. *J. Am. Chem. Soc.* **2008**, 130 (9), 2869-2876.

(78) Agustí, G.; Muñoz, M. C.; Gaspar, A. B.; Real, J. A. *Inorg. Chem.* **2009**, 48 (8), 3371-3381.

(79) Yasui, M.; Ishikawa, Y.; Ishida, T.; Nogami, T.; Iwasaki, F. *Acta Crystallogr. Sect. B Struct. Sci.* **2001**, *57* (6), 772–779.

(80) Plater, M. J.; Mark, M. R.; Slawin, A. M. Z. *Inorganica Chim. Acta* **2000**, *303* (1), 132–136.

(81) Funck, L. L.; Ortolano, T. R. *Inorg. Chem.* **1968**, *7* (3), 567–573.

Appendix

	L[1]	**L[2a]**
Empirical formula	$C_{12}H_8N_6$	$C_{14}H_{14}N_6O$
Formula weight	236.08	282.30
Temperature/K	119.99(14)	120.01(11)
Crystal system	monoclinic	monoclinic
Space group	I2/a	$P2_1/c$
a/Å	8.4077(3)	10.9701(3)
b/Å	9.8168(3)	14.2686(3)
c/Å	14.2828(5)	9.3654(3)
α/°	90	90
β/°	107.046(4)	114.236(4)
γ/°	90	90
Volume/Å3	1127.07(7)	1336.74(8)
Z	4	4
ρcalcg/cm3	1.351	1.4027
μ/mm-1	3.138	0.781
Radiation	CuKα (λ = 1.54184)	Cu Kα (λ = 1.54184)
2Θ range for data collection/°	12.966 to 147.02	8.84 to 148.76
Index ranges	-10 ≤ h ≤ 10, -9 ≤ k ≤ 11, -16 ≤ l ≤ 17	-13 ≤ h ≤ 13, -17 ≤ k ≤ 17, -8 ≤ l ≤ 11
Reflections collected	1927	8244
Independent reflections	1082 [Rint = 0.0157, Rsigma = 0.0170]	2704 [Rint = 0.0272, Rsigma = 0.0213]
Data/restraints/parameters	1082/0/84	2704/0/200
Goodness-of-fit on F2	1.458	1.378
Final R indexes [I>=2σ (I)]	R1 = 0.0489, wR2 = 0.1642	R1 = 0.0459, wR2 = 0.1546
Final R indexes [all data]	R1 = 0.0512, wR2 = 0.1670	R1 = 0.0487, wR2 = 0.1579
Largest diff. peak/hole / e Å-3	0.84/-0.19	0.35/-0.27

	L^7	**1a**
Empirical formula	$C_{12}H_9Br_2N_5$	$C_{24}H_{16}B_2F_8FeN_{12}$
Formula weight	380.04	701.96
Temperature/K	150.01	120.15
Crystal system	orthorhombic	triclinic
Space group	$P2_12_12_1$	P-1
a/Å	4.0781(4)	8.5664(6)
b/Å	17.7446(16)	16.7521(8)
c/Å	18.225(2)	19.3801(19)
α/°	90	95.278(6)
β/°	90	90.487(7)
γ/°	90	91.814(5)
Volume/$Å^3$	1318.9(2)	2767.8(4)
Z	4	4
$\rho_{calc}g/cm^3$	1.301	1.685
μ/mm^{-1}	0.084	5.248
Radiation	MoKα (λ = 0.71073)	CuKα (λ = 1.54184)
2Θ range for data collection/°	7.09 to 59.408	6.678 to 148.502
Index ranges	$-5 \le h \le 4, -24 \le k \le 20, -16 \le l \le 24$	$-10 \le h \le 10, -20 \le k \le 20, -23 \le l \le 23$
Reflections collected	5112	12882
Independent reflections	2957 [R_{int} = 0.0812, R_{sigma} = 0.1259]	12882 [R_{int} = ?, R_{sigma} = 0.1016]
Data/restraints/parameters	2957/0/77	12882/3/848
Goodness-of-fit on F^2	1.252	0.957
Final R indexes [I>=2σ (I)]	R_1 = 0.1033, wR_2 = 0.2366	R_1 = 0.0740, wR_2 = 0.1931
Final R indexes [all data]	R_1 = 0.1301, wR_2 = 0.2625	R_1 = 0.1126, wR_2 = 0.2102
Largest diff. peak/hole / e $Å^{-3}$	2.62/-2.75	1.04/-0.65

	1a	**1b**
Empirical formula	$C_{24}H_{16}B_2F_8FeN_{12}$	$C_{24}H_{16}Cl_2FeN_{12}O_8$
Formula weight	701.96	727.21
Temperature/K	290.00	120.10
Crystal system	monoclinic	monoclinic
Space group	P21	P21/c
a/Å	8.4937(4)	18.9858(8)
b/Å	39.2856(15)	8.6768(4)
c/Å	8.4930(3)	17.0037(7)
α/°	90	90
β/°	90.088(4)	91.848(4)
γ/°	90	90
Volume/Å3	2833.9(2)	2799.67(19)
Z	4	4
ρcalcg/cm3	0.101	1.259
μ/mm-1	0.12	1.631
Radiation	Diamond light source beamline I19 (λ = 0.6889)	CuKα (λ = 1.54184)
2Θ range for data collection/°	4.02 to 49.532	9.322 to 147.492
Index ranges	-9 ≤ h ≤ 9, -46 ≤ k ≤ 47, -10 ≤ l ≤ 10	-23 ≤ h ≤ 22, -10 ≤ k ≤ 10, -20 ≤ l ≤ 14
Reflections collected	11440	11835
Independent reflections	6865 [Rint = 0.1840, Rsigma = 0.2312]	5185 [Rint = 0.0568, Rsigma = 0.0720]
Data/restraints/parameters	6865/1/847	5185/0/424
Goodness-of-fit on F2	1.687	1.06
Final R indexes [I>=2σ (I)]	R1 = 0.2154, wR2 = 0.3941	R1 = 0.0648, wR2 = 0.1581
Final R indexes [all data]	R1 = 0.2235, wR2 = 0.4056	R1 = 0.0878, wR2 = 0.1712
Largest diff. peak/hole / e Å-3	4.80/-1.08	0.77/-0.57

	1c	**3**
Empirical formula	$C_{26}H_{16}F_6FeN_{12}O_6S_2$	$C_{24}H_{12}B_2Cl_4F_8FeN_{12}$
Formula weight	826.45	839.70
Temperature/K	119.99	120.00
Crystal system	monoclinic	monoclinic
Space group	P21/n	P21/n
a/Å	12.17821(15)	13.2457(3)
b/Å	20.3824(2)	19.2914(3)
c/Å	12.70519(15)	13.4811(2)
α/°	90	90
β/°	96.3503(11)	96.491(2)
γ/°	90	90
Volume/Å3	3134.35(7)	3422.72(11)
Z	4	4
ρcalcg/cm3	1.349	1.312
μ/mm-1	1.82	1.661
Radiation	CuKα (λ = 1.54184)	CuKα (λ = 1.54184)
2Θ range for data collection/°	8.236 to 147.258	8.036 to 148.554
Index ranges	-10 ≤ h ≤ 14, -17 ≤ k ≤ 25, -15 ≤ l ≤ 14	-16 ≤ h ≤ 16, -24 ≤ k ≤ 24, -16 ≤ l ≤ 16
Reflections collected	13823	27237
Independent reflections	5954 [Rint = 0.0222, Rsigma = 0.0269]	6746 [Rint = 0.0942, Rsigma = 0.0646]
Data/restraints/parameters	5954/0/458	6746/0/487
Goodness-of-fit on F2	1.355	1.39
Final R indexes [I>=2σ (I)]	R1 = 0.0497, wR2 = 0.1589	R1 = 0.0769, wR2 = 0.1969
Final R indexes [all data]	R1 = 0.0540, wR2 = 0.1636	R1 = 0.0845, wR2 = 0.2061
Largest diff. peak/hole / e Å-3	0.94/-1.13	0.81/-0.73

	5b	**7**
Empirical formula	$C_{28}H_{30}Cl_2FeN_{10}O_8$	$C_{24}H_{18}B_2Br_4F_8FeN_{10}$
Formula weight	760.10	991.54
Temperature/K	150.00	150.00
Crystal system	triclinic	triclinic
Space group	P-1	P-1
a/Å	9.5922(9)	13.8461(5)
b/Å	9.7535(10)	13.9875(6)
c/Å	18.307(2)	20.2371(11)
α/°	90.453(8)	101.519(4)
β/°	95.689(8)	108.183(4)
γ/°	90.892(8)	90.880(3)
Volume/Å^3	1704.1(3)	3635.9(3)
Z	2	4
ρ_{calc}g/cm^3	1.293	1.297
μ/mm^{-1}	0.324	0.179
Radiation	MoKα (λ = 0.71073)	MoKα (λ = 0.71073)
2Θ range for data collection/°	6.482 to 58.974	6.568 to 59.43
Index ranges	$-13 \le h \le 9$, $-13 \le k \le 10$, $-21 \le l \le 23$	$-14 \le h \le 19$, $-17 \le k \le 18$, $-28 \le l \le 25$
Reflections collected	9388	37466
Independent reflections	6324 [R_{int} = 0.0397, R_{sigma} = 0.0932]	17406 [Rint = 0.0473, Rsigma = 0.0690]
Data/restraints/parameters	6324/0/442	17406/0/919
Goodness-of-fit on F^2	2.008	2.962
Final R indexes [I>=2σ (I)]	R_1 = 0.1379, wR_2 = 0.3491	R1 = 0.1669, wR2 = 0.4521
Final R indexes [all data]	R_1 = 0.1722, wR_2 = 0.3608	R1 = 0.1821, wR2 = 0.4594
Largest diff. peak/hole / e Å^{-3}	2.69/-0.77	3.94/-2.56

	9	
Empirical formula	$C_{25}H_{19}Ag_2B_2F_8N_{13}O_2$	$C_{23}H_{13}F_{12}MnN_7O_6$
Formula weight	922.85	766.31
Temperature/K	120.00	119.99
Crystal system	triclinic	monoclinic
Space group	P-1	P21/n
a/Å	9.8239(7)	13.0198(3)
b/Å	12.1083(9)	16.4530(5)
c/Å	13.8819(8)	13.8821(2)
α/°	97.777(5)	90
β/°	110.059(6)	101.820(2)
γ/°	94.945(6)	90
Volume/Å3	1521.16(19)	2910.68(12)
Z	7	13
ρcalcg/cm3	2.699	1.319
μ/mm-1	19.072	1.52
Radiation	CuKα (λ = 1.54184)	CuKα (λ = 1.54184)
2Θ range for data collection/°	6.886 to 148.018	10.048 to 148.694
Index ranges	-8 ≤ h ≤ 11, -15 ≤ k ≤ 14, -16 ≤ l ≤ 16	-14 ≤ h ≤ 15, -17 ≤ k ≤ 17, -15 ≤ l ≤ 16
Reflections collected	11259	7627
Independent reflections	5697 [Rint = 0.0372, Rsigma = 0.0509]	4201 [Rint = 0.0299, Rsigma = 0.0377]
Data/restraints/parameters	5697/0/469	4201/0/382
Goodness-of-fit on F2	0.955	1.638
Final R indexes [I>=2σ (I)]	R1 = 0.0431, wR2 = 0.1241	R1 = 0.1098, wR2 = 0.3368
Final R indexes [all data]	R1 = 0.0560, wR2 = 0.1346	R1 = 0.1179, wR2 = 0.3534
Largest diff. peak/hole / e Å-3	1.36/-0.66	2.13/-1.17